Characterisation of Phase Noise for the Preparation of Atoms in the Motional Ground State

Masterarbeit von Isabella Rahel Boventer

Angefertigt im

**Institut für Angewandte Physik der
Rheinischen Friedrich-Wilhelms Universität Bonn**

Vorgelegt der

Mathematisch − Naturwissenschaftlichen Fakultät

der Rheinischen Friedrich − Wilhelms Universität Bonn

September 2014

Supervisors of this master thesis:

First: Prof. Dr. Dieter Meschede

Second: Prof. Dr. Hans Kroha

Contents

1

Introduction

Physics can be regarded as the general study of nature, including matter, motion and energy [1]. The research in this field can be characterized by the scientific method, which enables to test the validity of a physical theory [2]. From that point of view experiments measure a physical quantity by comparing it with a standard which is considered as a true value[3]. The deviation of the measured value from the true value is denoted as a measurement error. Further the uncertainty of a measurement is defined as the "dispersion of the values which could be reasonably attributed to the measurement" [3]. Next to systematic errors which are biases in measurements, randomly distributed fluctuations of a physical quantity under test contributed to the uncertainty of a measurement. It is also called noise and can originate from technical electronical noise due to the measurement devices such as thermal(Johnson) noise [4]. On the atomic and subatomic level quantum mechanics has to be used for a description of the processes on these scales. [5]. Consequently, measurements of properties of quantum states are limited by quantum noise. Quantum noise can be regarded as a consequence of the Heisenberg uncertainty principle [6]. It can occur in the form of amplitude or phase fluctuations of an oscillating electrical field such as laser light and is called intensity or phase noise respectively [6]. Referring to the latter phase noise is an issue in communications, signal processing and quantum systems [7], [4]. It describes randomly distributed temporal fluctuations in frequency domain and is characterized by a spectral decomposition of the total power into intervals of noise frequency [8], that is also called the power spectral density [9]. Phase noise can affect quantum states which relay on a well defined phase relation between the involved states. Thus,laser light, which is described as a coherent stae and correlated states are sensitive to phase noise [5]. This could destroy the well defined quantum state and lead to decoherence [10]. In terms of the density matrix description this is classified as an evolution from a pure state into a statistical mixture [11]. Therefore it has to be considered in the realization of full control over single quantum systems. Due to the progress in the development of cooling and trapping techniques of single particles such as ions([12]) and neutral atoms(i.e [13]) the control and manipulation of single internal particles states became possible ([14, 15, 16]). One application is to simulate quantum behaviour using single particles and therefore the next step is the realization of the correlation of two quantum states [17].

In that sense we are currently working on the realization of a controlled interaction between two neutral cesium atoms trapped in an state dependent optical lattice ([18]). Later on, this would allow to measure the degree of indistinguishability of the involved atoms [19]. It will pave the way for the creation of entanglement with neutral atoms via coherent cold collisions [20]. These systems are promising candidates because they combine the advantages of neutral atoms such as long coherence times [21] with the high degree of ex-

perimental control of the atoms in an optical lattice [22]. For our experiments the atoms are prepared in the hyperfine states $|F = 4, m_F = 4\rangle \equiv |\uparrow\rangle$ and $|F = 3, m_F = 3\rangle \equiv |\downarrow\rangle$ of the D2 line of atomic cesium. We are able to address and manipulate the atoms individually with single site resolution. Further we can employ state dependent transport to change the position of the atoms [23, 14, 21].

However, a realization of a controlled interaction requires that the positions of the atoms can be well resolved and the atoms are prepared in the three dimensional motional ground state [24]. The atoms can be cooled into the motional ground state along the optical lattice by employing microwave sideband cooling [23]. Due to the required relative phase shift between state dependent lattice potentials microwave sideband cooling is not possible in the radial direction [25]. Therefore for cooling into the radial plane a setup for Raman sideband cooling has been assembled in our group. Considering that the driving source of the trapping potentials and the Raman sideband cooling techniques are laser beams and the atoms have to be prepared in well defined, i.e pure states, fluctuations from the beams or decoherence processes result naturally into phase noise. Therefore I characterized two different sources of phase noise, which can limit the successful preparation of atoms into the motional ground state. Since Raman sideband transitions couple different motional states of two ground states with a small energy spacing in a two photon process [16] the frequency between the Raman lasers has to precisely match the hyperfine energy splitting. Therefore, the phase has to be stabilized by using an optical phase lock loop(OPLL), which I characterized by measureing the phase noise (Section 2.5). Embedded in a description of the Raman setup the results will be presented in Chapter 2. The successful implementation of this setup into the experimental apparatus allows now to cool around 56% of the atoms into the three dimensional ground state.[1](Section 2.7). In Chapter 3. I will present a characterization of the common mode optical phase noise of the optical lattice. As stated above such phase noise could in principle lead to heating, decoherence or an uncertainty in the determination of the position [26, 27]. It can be due to mechanical instabilities,for example. Other sources of noise, such as beam pointing instabilities from the dipole trap lasers have been already well studied and can be found in Ref.[28] and Ref. [29]. Any noise signal can be regarded as a beat signal from the undisturbed source with the fluctuation [6]. Accordingly I assembled an interferometer to measure this noise which will be described in Sec.3.2. The influence from both the fast(Section.3.5) and the slow (Section.3.6) fluctuating component was studied. It will be shown that the insertion of a slow feedback loop can be used for a stabilization of the slow drifts. Chapter 4. covers first considerations regarding a Quadrature interferometer in order to study further the phase noise of the optical lattice.

---

[1]Measurement results shown with kind permission by C. Robens

2

Setup for Raman Sideband Cooling with Phase Noise Characterisation

In order to study Bose statistics by fourth order interference effects [18, 30] and a reproducible atom atom interaction the atoms have to be in the motional groundstate in all spatial dimensions. [24] The technique of Raman sideband cooling relies on a change in the atomic momentum when an atom interacts with Raman light fields [16]. A general Raman process is a two photon process which leads to transitions between two states by means of a third, virtual state, which is far off resonant to the excited state [31]. In a good approximation atoms which are confined in a standing wave potential of an optical lattice populate quantized energy states; the motional states of a harmonic oszillator. Consequently, Raman sideband transitions tuned to the first blue sideband (Sec.2.2) induce transitions to lower motional energy states until the motional ground state is reached. It represents a dark state for cooling. Along the axial direction the atoms were cooled into the motional ground state with a probability $P_0 \approx 97\%$ by microwave sideband cooling [23]. In the radial direction microwave sideband cooling is not possible(c.f. [25]). Therefore a setup for employing Raman sideband transitions to cool to the radial motional ground state is introduced. First an overview about the general concepts and prerequisites for Raman sideband transitions will be described. Then the assembly of the Raman setup including a measurement for the characterization of the phase stability of the Raman transitions is presented in Sec.2.4.2. Additionally the demonstration of cooling into the three dimensional ground state is displayed in Sec.2.7.

2.1   The optical dipole potential

The optical dipole potential arises from the interaction of a far detuned radiation field with an induced atomic dipole moment. This leads to a conservative dipole force [32]. Depending on the detuning this results in attractive ($\Delta < 0$) or repulsive($\Delta > 0$) potentials.
In the semiclassical picture an atom can be described as an effective two level quantum system which interacts with a classical radiation field. Fig. 2.1 shows the driving frequency of the light field which is detuned by Δ from the resonant transition frequency ω_0. The states $|g\rangle$ and $|e\rangle$ denote the ground and the excited state and represent the basis states of the system. In the dipole approximation ($\lambda_{\text{field}} \gg$ x, with x denoting the spatial extension of
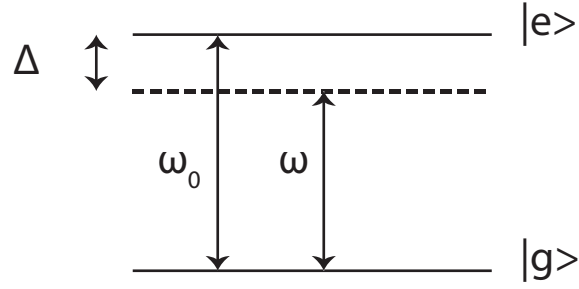
Fig. 2.1: Illustration of the atom as a two level quantum system with the groundstate $|g\rangle$ and excited state $|e\rangle$. The frequency of the resonant transition is denoted by ω_0, the frequency of the light field by ω and the detuning defined as $\Delta \equiv \omega - \omega_0$

the atom, a monochromatic driving field can be written as:

$$ (2.1) $$

$$ \mathbf{E}(\mathrm{t}) = \hat{\varepsilon} \mathrm{E}_0 \cos(\omega \mathrm{t}) \quad \begin{aligned} &\hat{\varepsilon} : \text{unit polarization vector} \\ &\mathrm{E}_0 : \text{field amplitude} \\ &\omega : \text{field angular frequency} \end{aligned} $$

A decomposition into the positive and negative oscillation frequencies yields:

$$ \mathbf{E}(\mathrm{t}) = \frac{\hat{\varepsilon} \mathrm{E}_0}{2} (e^{-i\omega t} + e^{i\omega t}) \tag{2.2} $$
$$ = \mathbf{E}^+(\mathrm{t}) + \mathbf{E}^-(\mathrm{t}). \tag{2.3} $$

The time evolution is given by the Schrödinger Equation:

$$ \mathrm{H}\Psi(\mathrm{r,t}) = i\hbar \frac{\partial}{\partial t}\Psi(\mathrm{r,t}) \tag{2.4} $$

The Hamiltonian H is composed of the unperturbed Hamiltonian H_0, describing the free evolution of the system with energy eigenvalues $\hbar\omega_0$ and the interaction hamiltionian H_{int}:

$$ \mathrm{H} = \mathrm{H}_0 + \mathrm{H}_{\text{int.}} \tag{2.5} $$
$$ \mathrm{H}_0 = \hbar\omega_0 |e\rangle \langle e| $$
$$ \mathrm{H}_{\text{int.}} = -\mathbf{d} \cdot \mathbf{E} = -e\mathbf{r} \cdot \mathbf{E} $$

The derivation of the dipole potential follows the one from Chapter 5.) of Ref.[33] The energy of the ground state is set to zero, and the dipole operator expressed in terms of lowering and rising operators $\sigma = |g\rangle \langle e|$ and $\sigma^\dagger = |e\rangle \langle g|$, respectively.

$$ \mathbf{d} = \langle g| \mathbf{d} |e\rangle (\sigma + \sigma^\dagger), \tag{2.6} $$

where the phase of the dipole matrix element is assumed to be real.
Since $\langle \sigma \rangle = \langle |g\rangle \langle e| \rangle \propto e^{-i\omega_0 t}$, the dipole operator can be decomposed into two oscillating parts, as well. An insertion of these decompositions into Eq.**??** yields in the rotating wave approximation (RWA) [1] the interaction Hamiltonian can be written as:

$$ \mathrm{H}_{\text{int.}} = \frac{\hbar}{2} (\Omega^* \sigma e^{i\omega t} + \Omega \sigma^\dagger e^{-i\omega t}), \tag{2.7} $$

---

[1] Since $|\Delta| \equiv |\omega - \omega_0| \ll \omega + \omega_0$ the fast oscillations are averaged to zero, allowing a focus on the slow dynamics of the system

where Ω denotes the Rabi frequency. It describes the coupling strength between the ground and the excited state and is defined as the transition matrix element of the dipole operator:

$$\Omega \equiv -\frac{2}{\hbar} \langle g| \, \hat{\boldsymbol{\varepsilon}} \mathbf{d} \, |e\rangle \, E_0^+ \tag{2.8}$$

The atomic state is now a superposition from the ground and the excited state (only dipole moment for mixed states) , with the time dependence in the coeffients c_i.

$$|\Psi\rangle = c(t)_g \, |g\rangle + c(t)_e \, |e\rangle \tag{2.9}$$

By means of the transformation into a rotating frame we do not consider fast rotations in the equation of motion. The amplitude of the slowly varying excited state is thus defined as: $\tilde{c}_e = c_e \exp^{i\omega t}$. In the rotating frame (RF) approximation the Hamiltonian is described by:

$$H^{RF} = H_0^{RF} + H_{int.RF} \tag{2.10}$$

$$= -\hbar\Delta \, |e\rangle \, \langle e| + \frac{\hbar\Omega}{2}(\sigma + \sigma^\dagger). \tag{2.11}$$

$$\tag{2.12}$$

The solution of the Schrödinger equation results in to a set of equations of motions:

$$\partial_t c_g = -i\frac{\Omega}{2}\tilde{c}_e \tag{2.13}$$

$$\partial_t \tilde{c}_e = i\Delta\tilde{c}_e - -i\frac{\Omega}{2}c_g \tag{2.14}$$

The solution of these equation describes Rabi flopping [31]. Accordingly, the population is oscillating between the ground and the excited state with the generalized Rabi frequency $\tilde{\Omega} = \sqrt{\Omega^2 + \Delta^2}$ [31]. The time evolution of the atom-field dynamics is described by:

$$c_g(t) = e^{\frac{i\Delta t}{2}} \left[c_g(0)\cos(\frac{\tilde{\Omega}t}{2}) - \frac{i}{\tilde{\Omega}}[\Delta c_g(0) + \Omega c_e(0)]\sin(\frac{\tilde{\Omega}t}{2}) \right]$$

$$\tilde{c}_e(t) = e^{\frac{i\Delta t}{2}} \left[\tilde{c}_e(0)\cos\left(\frac{\tilde{\Omega}t}{2}\right) + \frac{i}{\tilde{\Omega}}[\Delta\tilde{c}_e(0) - \Omega\tilde{c}_g(0)]\sin\left(\frac{\tilde{\Omega}t}{2}\right) \right]$$

Now the dipole force can be calculated in a non perturbative analysis. In the Heisenberg representation [34], the total force is related to the interaction Hamiltonian via:

$$\mathbf{F} = \partial_t \mathbf{p} = \frac{i}{\hbar}[H, \mathbf{p}] = -\nabla H_{int.} \tag{2.15}$$

With the notation $\Omega(r) = |\Omega(r)|e^{i\phi(r)}$, where r denotes the mean atomic position in the semiclassical approach the mean force can be written as a sum from two contributions to the dipole force. The first term in Eq.2.16 corresponds to the dipole and the second to the radiation pressure force.

$$\langle F \rangle = \langle F_{dip.} \rangle + \langle F_{rad.} \rangle \tag{2.16}$$

Introducing the saturation parameter s [2] ,

$$s(r) = \frac{|\Omega(r)|^2}{2|\left(\frac{\Gamma}{2}\right)^2 + \Delta^2|} \tag{2.17}$$

---

[2]This expression arises from the density matrix formalism and the steady state solution of the optical Bloch equations (OBE), which describe the temporal evolution in terms of the density matrix [35]

and the relation $\langle \mathbf{F}_{\text{dip.}} \rangle = -\nabla V_{\text{dip.}}$ yields the solution for the dipole potential [33, 32]:

$$U_{\text{dip.}} = \frac{\hbar\Delta}{2}\log\left(1 + \frac{I/I_{\text{sat.}}}{1 + 4(\Delta/\Gamma)^2}\right) \tag{2.18}$$

In the case off far off resonant interaction this simplifies to:

$$U_{dip.} = \frac{3\pi c^2}{2\omega_0^3}\left(\frac{\Gamma}{\Delta}\right)\mathbf{I}(\mathbf{r}) \tag{2.19}$$

Hence atoms are attracted into the light field towards the intensity maxima for red detuned light ($\Delta < 0$) and for blue detuned light ($\Delta > 0$) repelled out of the field towards intensity minima. In addition, the dipole potential corresponds to an light induced shift of the atomic energy levels. The energy eigenvalues of the full Hamilitonian including the interaction do not correspond to $H_0|\Psi\rangle = \hbar\omega_0|\Psi\rangle$. The new Hamiltonian is represented by:

$$H = \begin{pmatrix} -2\Delta & \Omega \\ \Omega & 0 \end{pmatrix}. \tag{2.20}$$

A diagonalization yields the new energy eigenvalues $E_{g,e} = \frac{\hbar}{2}\left(-\Delta \pm \tilde{\Omega}\right)$. In the limit $\Omega \ll |\Delta|$ and using $\frac{I}{I_{\text{sat.}}} = 2\frac{\Omega^2}{\Gamma^2}$ one obtains:

$$\Delta E = \pm U_{dip.} \tag{2.21}$$

Therefore the light shifted ground state of a two level atom represents the optical dipole potential trapping the atoms.

2.1.1   Multilevel atoms

In reality an atom exhibits a multilevel energy struture. The light field couples to various states, where the coupling strength is characterized by the corresponding Rabi frequency. By means of the Wigner-Eckhart Theorem [36] the dipole matrix element can be decomposed into a product of a reduced matrix element and Clebsch-Gordon coefficients (c_{ij}). The latter ones take, for instance, polarization and the coupling strengths between sub energy levels into account.

$$\langle F, m_F | d | F', m_{F'} \rangle = \langle F \| d \| F' \rangle \cdot c_{ij} \tag{2.22}$$

For the resulting dipole potential all contributions have to be summed and weighted by their relative coupling strength. [32].

$$U_{\text{dip.}} = \frac{3\pi c^2 \Gamma}{2\omega_0^3} Ix \sum_j \frac{c_{ij}^2}{\Delta_{ij}}, \tag{2.23}$$

where i and j denote the sublevels of electronic ground and excited state.
Alkali atoms are well suited for cooling and trapping experiments. They exhibtit long lived ground states and closed electronic shells with one electron, which simplifies the description of the coupling [21]. For the case of cesium atoms in a red detuned trap the dominant contributions are the D1 and the D2 lines, e.g the transitions from the $6^2S_{1/2}$ doublet to the state $6^2P_{1/2}$ and $6^2P_{3/2}$ respectively.[37]. This leads to the general result ($\Delta_{\text{HFS}} \ll \Delta_{D_i}$) [32]:

$$U_{trap.} = \frac{\pi c^2 \Gamma}{2\omega_0^3}\left(\frac{2 + \xi g_F m_F}{\Delta_{D2,F}} + \frac{1 - \xi g_F m_F}{\Delta_{D1,F}}\mathbf{I}(\mathbf{r})\right), \tag{2.24}$$

$6^2P_{3/2}$ ___

D2-line 852 nm

F=4 ___

$6^2S_{1/2}$ ___

ω_0=9.19 GHz

F=3 ___

$m_F = 0$

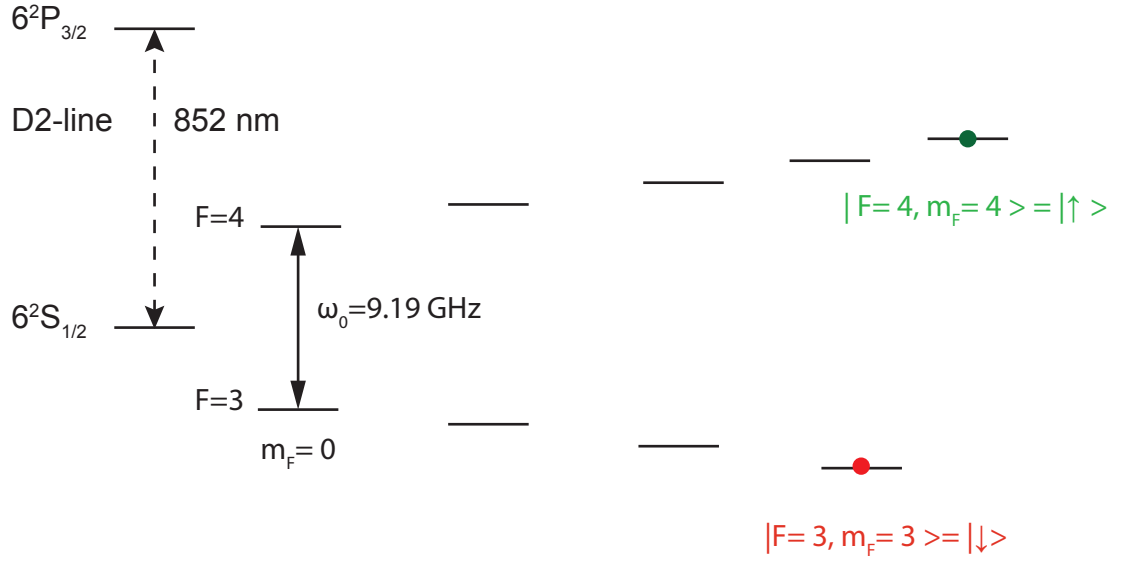$|F=4, m_F=4> = |\uparrow>$

$|F=3, m_F=3> = |\downarrow>$

Fig. 2.2: Illustration of the HFS structure of ^{133}Cs of the $6^2S_{1/2}$ state with the choice of the two basis states for our experiment which are the outermost Zeeman sublevels $|F=4, m_F=4\rangle \equiv |\uparrow\rangle$ and $|F=3, m_F=3\rangle \equiv |\downarrow\rangle$.

where $\xi \in (0, \pm 1)$ denote the polarisations $(\pi, \sigma^{\pm})$ of the light field, g_F the Landé factor and $\Delta_{D_i,F}$ the corresponding detunings. In the experiment which will be presented in Sec. 2.6 we use the outermost hyperfine groundstates of the cesium D2-line. These states represent our two qubit states for the description of the atom as a two level quantum(quasi spin 1/2) system. The corresponding term scheme is illustrated in Fig. 2.2.

2.1.2 Standing wave potential

The optical lattice in our experiment is created by two counterpropagating, Gaussian laser beams with linear polarization. This leads to a Gaussian intensity profile and yields a dipole potential of the form [38]. Thus, the optical latice is a periodic pattern of trapping potentials.

$$U_{\text{trap.}}(\mathbf{r}) = -U_0 \frac{\omega_0^2}{\omega(z)^2} e^{-\frac{2\rho^2}{\omega(z)^2}} cos^2(\text{kz}), \qquad (2.25)$$

where U_0 denotes the maximum trap depth.[38].

2.1.3 The state dependendent optical lattice

A controlled interaction between two bosonic cesium atoms requires an individual control of the atoms in different spin states. For a special choice of the detuning from the cesium D2-line which is given at a wavelength of 865.9 nm the optical lattice potential becomes state dependent. The contributions to the potential cancel for m= $\pm\frac{1}{2}$ because the states in $62^P_{3/2}$ and $62^P_{1/2}$ are equally detuned at that wavelength from resonance but with different signs of the detuning. The remaining transitions with circular polarization are red detuned, which leads to an attractive, state dependent potential [38, 23]. As it is also shown in Fig.2.3 the atoms are depending on their state either exclusively trapped by the σ^+ or the σ^- polarized component of the lattice potential. However we use the cesium hyperfine states $|F=3, m_F=3\rangle \equiv |\downarrow\rangle$ and $|F=4, m_F=4\rangle \equiv |\uparrow\rangle$ as our qubit states. In this case
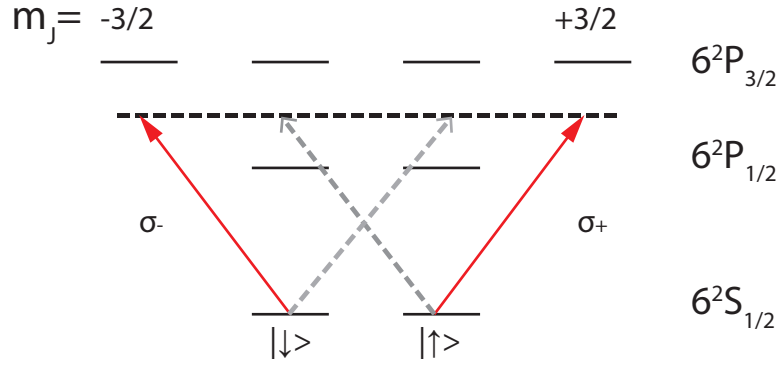
Fig. 2.3: The 'mixed' polarization components of the potential cancel by being equally blue(red) detuned to the 'magic' wavelength of 865.9 nm. The remaining dipole transitons are red detuned and lead to an attractive potential [adapted from [23]]

the atoms in $|\uparrow\rangle$ are still only trapped by the σ^+ polarized component of the potential, but the atoms in $|\downarrow\rangle$ are now trapped by a potential which also contains a small contribution from the σ^+ polarized component. The relative weights are given by the Clebsch-Gordan coefficients.

$$U_{|\uparrow\rangle} = U_{\sigma^+} \tag{2.26}$$
$$U_{|\downarrow\rangle} = \frac{1}{8}U_{\sigma^+} + \frac{7}{8}U_{\sigma^-}$$

3

2.2 The motional groundstate

As mentioned the motional ground state it crucial for a reproducible atom-atom interaction, for instance. Using a Taylor expansion for the expression of the potential in Eq.2.25 reveals that each potential well of the optical lattice can be approximated by the potential of a harmonic oscillator. An atom which is bound in such a potential undergoes an oscillatory movement with frequency $\omega_{\mathrm{mot.}}$. The energy states are quantized with an energy of $E_{\mathrm{mot.}} = \hbar\omega_{\mathrm{mot.}}\left(n+1/2\right))$. These states are the motional states. Without any additional cooling the motional states are occupied following a thermal Boltzmann distribution and do not populate all the ground state. Each internal state of an atom is dressed with the motional states. In the description of an atom as a two level system the motional states can be changed by inducing transitions between different motional states in $|\uparrow\rangle$ and $|\downarrow\rangle$ (c.f.Fig.2.2). The transition on the resonance frequency ω_0 between the ground and the excited state does not change the motional state and is denoted as the carrier transition. If the linewidth Γ of the corresponding transition is much smaller than the motional frequency the sideband transitions can be resolved ($\Gamma \ll \omega_{\mathrm{mot.}}$). Accordingly sidebands appear in the absorption spectrum as it is illustrated in Fig.2.4. The sidebands appear at center frequencies $\omega_0 \pm \chi\omega_{\mathrm{mot}}$, where χ corresponds to the change of the motional state an is called the nth sideband.

---

[3]Referring to Eq. 2.25 U_0 denotes the maximal depth, $\omega(z)$ the beam radius of a Gaussian beam.
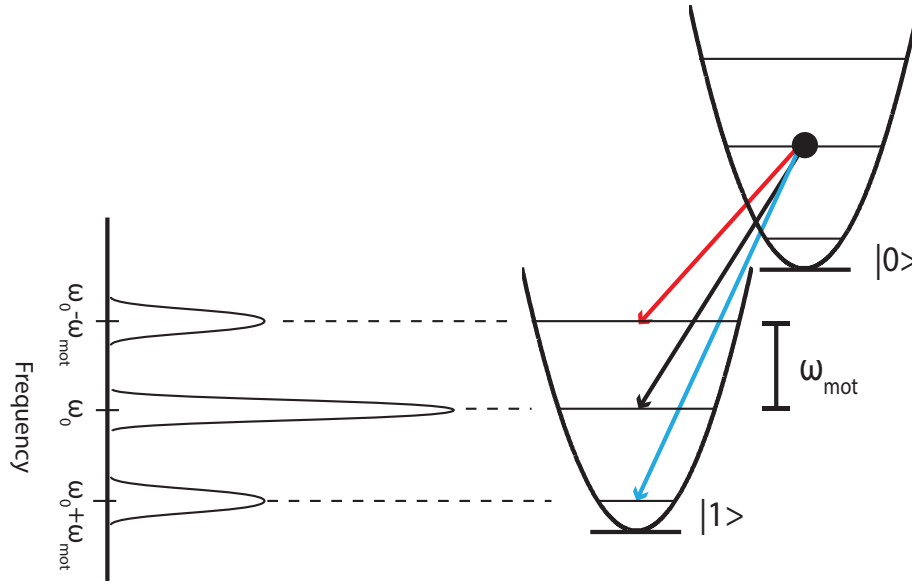
Fig. 2.4: Illustration of sideband transitions coupling different motional states of a two level atom in a harmonic potential. In the absorption spectrum this results in the appearence of sidebands at a distance $\pm\omega_{mot.}$ from the carrier transition with frequency ω_0 [adapted from [39]]

2.2.1 Lamb-Dicke Regime

In order to effectively cool an atom into its motional ground state diffusion to higher orders of motional states should be avoided. Therefore it is convenient to apply sideband cooling in the Lamb-Dicke Regime where transitions to higher orders of sidebands are strongly suppressed. In the Lamb-Dicke Regime the spread of the atomic ground state (n=0) wavefunction is much smaller than the wavelength of the cooling transition [40]. This is characterized by $\eta \ll 1$, where η represents the Lamb-Dicke parameter. It is defined as:

$$\eta = \mathrm{kx}_0 = \mathrm{k}\sqrt{\frac{\hbar}{2m\nu}}, \tag{2.27}$$

where x_0 denotes the spread of the wavefunction depending of the mass m of the atom and the motional frequency ν. If the sidebands are resolved and the Raman lasers are tuned such that transitions of the type $|b,n+\chi\rangle \to |a,n\rangle$ are in resonance ($\Delta \approx \chi\nu$) the basis states and the motional states become coupled. When the motional state undergoes a transition of the type $|b,n+1\rangle \leftrightarrow |a,n\rangle(|b,n-1\rangle \leftrightarrow |a,n\rangle)$ it is a transition on the first blue(red) sideband. The Lamb-Dicke parameter is also related to the coupling strength. The corresponding Rabi frequency yields:

$$\Omega_{n,n+\chi} \propto \Omega_0 \eta^{|\chi|}, \tag{2.28}$$

where Ω_0 denotes the Rabi frequency of the carrier [41] and $\chi \in \mathbb{Z}$ the order of the sideband. According to Eq.2.28 higher order sideband transitions are strongly suppressed and the interaction is dominated by the carrier transition and the first red and blue sideband respectively. Following Ref. [40] the corresponding Rabi frequencies are:

$$|e,n\rangle \leftrightarrow |g,n\rangle : \Omega_0 \tag{2.29}$$
$$|e,n\rangle \leftrightarrow |g,n+1\rangle : \Omega_0\sqrt{n+1}\eta$$
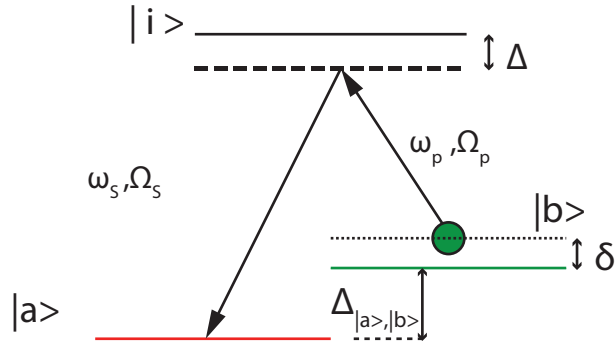$$|e,n\rangle \leftrightarrow |g,n-1\rangle : \Omega_0\sqrt{n}\eta$$

Fig. 2.5: The application of coherent Raman transitions couples two states $|a\rangle$ and $|b\rangle$ by means of an virtual state $|i\rangle$ in a two photon process. The virtual state is far detuned from resonance in order to avoid excitation.

2.2.2 Ground state population

The mean occupation of a motional state is characterized by the mean occupation number n̄. Following Ref.[42, 40] a comparison of the transition probability to the blue or red sideband of an atom in $|\uparrow, n\rangle$ allows the determination of n̄. The probabilities are probed by a Raman pulse for instance which is tuned to either χth sideband. One measures the surviving probability in $|\uparrow, n\rangle$ and infers $P_{|\chi\rangle}^{bsb} = 1 - P_{|\uparrow\rangle}^{bsb}$ and $P_{|\chi\rangle}^{rsb} = 1 - P_{|\uparrow\rangle}^{rsb}$ respectively. Defining the ratio R between the relative height of the sideband peaks yields for the mean occupation number:

$$R = \frac{P_{|\chi\rangle}^{bsb}}{P_{|\chi\rangle}^{rsb}} = \frac{\bar{n}}{\bar{n}+1} \tag{2.30}$$

$$\bar{n} = \frac{R}{1-R} \tag{2.31}$$

Then the probability that an atom is in the motional ground state after cooling can be calculated by:

$$P_0 = \frac{1}{1+\bar{n}} \tag{2.32}$$

2.3 Raman Transitions

General Raman process
Raman transitions couple two atomic states coherently in a two photon process by means of a virtual state which is detuned from the third, excited state. This configuration is also known as a Lambda-System. Like it is shown in Fig.2.5 the atom, which is prepared in state $|b\rangle$ is pumped by the Raman pump beam with frequency ω_p and Rabi frequency Ω_p to the virtual state. The subsequent application of the Raman stokes beam transfers the atom into the other basis state denoted by $|a\rangle$ by stimulated emission with frequency ω_S and Rabi frequency Ω_S. The temporal evolution of the propability amplitudes[4] in the corresponding states can be calculated in a similar manner to the case of the two level system. Accordingly by using the 'adiabatic elimination' approximation the population in the excited stated averages to zero [43]. Hence, this system can be described as an effective two level system

---

[4]Following the density matrix formalism, the square of the probability amplitude yields the population in the resepective state
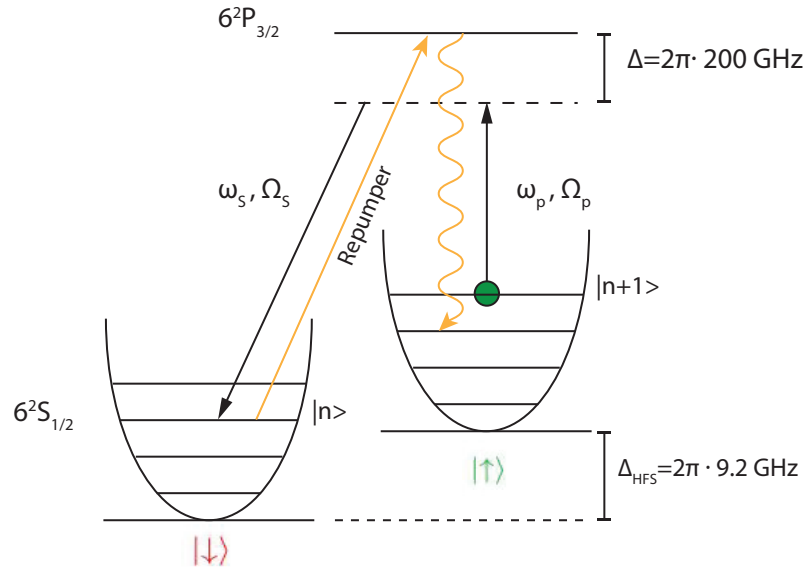
Fig. 2.6: Raman sideband transitions between the basis states of our experiment denoted by $|\uparrow\rangle$ and $|\downarrow\rangle$. The Raman pump laser is tuned to the first blue sideband which lowers the motional state by one when the atom is transferred into $|\downarrow\rangle$. For cooling a repumper and spontaneous emission transfer the atom into the initial state.

with a Rabi frequency Ω_{eff}[37]:

$$\Omega_{\text{eff.}} = \frac{\Omega_{RP} \cdot \Omega_{RS}}{2\Delta} \tag{2.33}$$

Change of momentum

The momentum transfer from the interaction of the atom with the radiation field in the Raman process yields $\Delta k = k_p - k_s$ [5]. The Lamb-Dicke parameter is now written as $\eta = \Delta k x_0$. Thus in the Lamb-Dicke regime the momentum of the atom is in good approximation not changed due to photon recoil but only due to the change of the motional state in sideband transitions. Therefore resolved Raman sideband cooling allows cooling below the recoil limit [16].

2.3.1 Raman sideband cooling

The qubit states $|\uparrow\rangle$ and $|\downarrow\rangle$ are long lived states. This results in the resolution of sidebands since the condition $\Gamma \ll \omega_{\text{mot.}}$ is fulfilled. The atoms are initially prepared by optical pumping in the $|\uparrow, n+1\rangle$ state. (Fig. 2.6). The Raman beams are both far off resonant to the transition of the cesium D2-line and couple both states coherently with the effective Rabi frequency. (c.f Fig.2.2). Furthermore the hyperfine energy splitting between both qubit states corresponds exactly to the frequency difference between the Raman laser beams.

Since the process starts in the energetically higher state this process can be used for cooling in the motional levels when the frequency difference, that is $\Delta\omega = \omega_p - \omega_s$, is tuned to the first blue sideband transition. Then atoms moving with a higher frequency $\omega + \Delta\omega$ are in resonance with this transition. Hence, the atoms are transferred to a lower motional state in $|\downarrow\rangle, n$ by the corresponding momentum kick Δk. In order to reach the motional ground

---

[5]$k_p(k_s)$ denotes the recoil the atom experiences from the interction with the Raman pump(stokes) laser
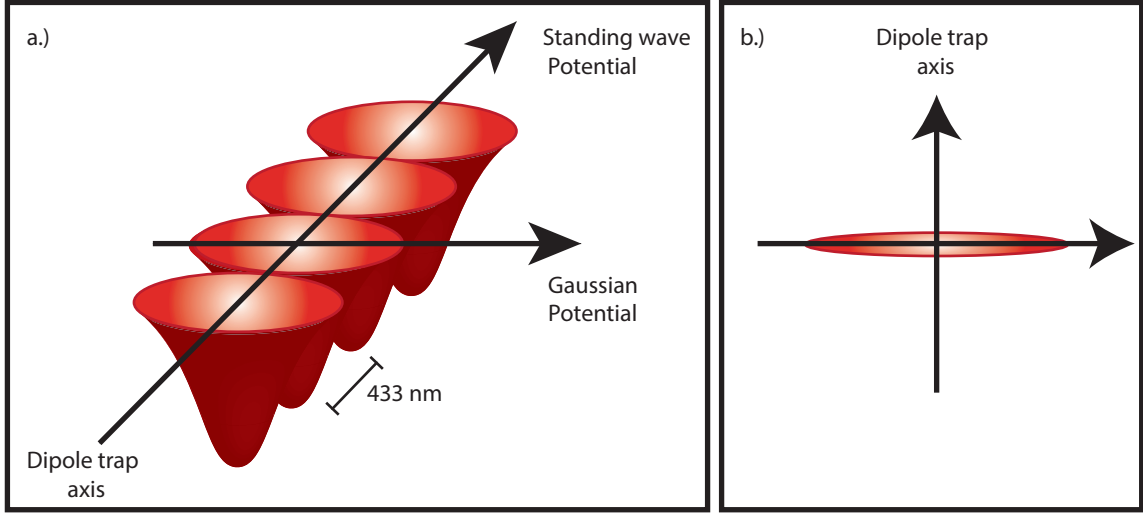
Fig. 2.7: Graphic illustration of the different confinement in axial and radial direction. b.) shows the top view for better illustration.

state the atom has to be brought back into the initial state. Referring to Fig.2.6 an additional repumper transfers the atom into the third, excited state. Via spontaneous emission the atom decays back to the initial internal state but with a motional state lowerered by one . Since the Raman sideband transitions are employed in the Lamb-Dicke Regime sideband transitions to higher orders are strongly suppressed (c.f. Fig.2.4) and the motional state remains unaltered. This process continues until the motional ground state is reached since it represents a dark state for the Raman beams [31]. There, the atoms do not interact any more with the Raman light fields.

2.3.2 Axial and radial confinement

Each potential well in the optical lattice can be approximated by a cylindrical harmonic oscillator. As it is illustrated in Fig. 2.7 the confinement along the dipole trap, that is the axial direction, is much higher than the confinement in radial direction. The trapping frequencis in the axial and radial respectively direction are:

$$\Omega_{\text{axial}} = 2\pi \sqrt{\frac{2U_0}{m_{\text{Cs.}} \lambda^2}} \tag{2.34}$$

$$\Omega_{\text{radial}} = \sqrt{\frac{4U_0}{m_{\text{Cs.}} \omega_{g0}^2}}, \tag{2.35}$$

where ω_{g0} denotes the beam waist of the Gaussian laser profile. Accordingly the confinement in the radial direction is only given by the Gaussian profile from the laser beam while in axial direction the atoms are trapped in the state dependent standing wave potential. The corresponding Lamb-Dicke parameter can be calculated as well. With a cesium mass $m = 2.2 \cdot 10^{-25}$ kg, a beamwaist of ω_{g0} at the atoms' position and a photon recoil energy of $\omega_r = 2\pi \cdot 2\,\text{kHz}$ ([39]) yields without any further confinement [25] :

$$\Omega_{\text{axial}} \approx 2\pi \cdot 110\,\text{kHz} \rightarrow \eta \approx 0.13$$
$$\Omega_{\text{radial}} \approx 2\pi \cdot 1\,\text{kHz} \rightarrow \eta \approx 1.41$$

In order to cool the atoms by resolved Raman sideband transitions effectively an operation in the Lamb-Dicke Regime ($\eta \ll 1$) has to be realized first. Thus the confinement in the
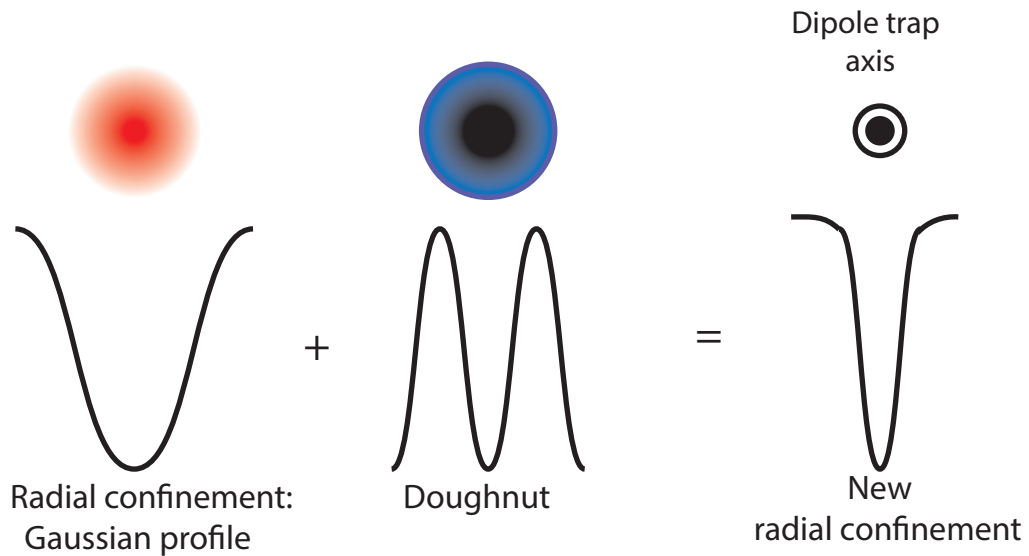
Fig. 2.8: Implementation of a doughnut shaped blue detuned laser beam increases the radial confinement. b.) The confinement has been increased compared to Fig.2.7

radial direction has to be increased.

Doughnut beam

This is achieved by shining in an additional blue detuned hollow beam, called doughnut beam, along the axis of the dipole trap. As it is displayed in Fig.2.8 the overlap increases the radial confinement. Following Ref.[44] and [45], where major contributions have been done, the doughnut beam is generated by the combination of a Gaussian laser beam and a spiral phase plate (SPP). This special lens imprints a phase pattern depending on the azimuthal angle of the Gaussian beam. [44]. According to the Fresnel-Huygens principle [46] the SPP acts as a disturbing wavefront where every point acts a new point source. These sources interfere mutually and at a certain distance destructive interference generates a dark center [45]. The detuning of this beam leads to a repulsive force which drags the atoms into the region with low intensity, that is the dark center.. This results in a trap frequency of $\Omega_{\text{radial}} \approx 2\pi \cdot 20\,\text{kHz}$ and a Lamb-Dicke parameter of $\eta \approx 0.31$, which enables efficient Raman sideband cooling. [6]

2.4 Stabilization of the Phase

Phase noise is characterized as the representation of rapid temporal fluctuations in the frequency domain [7]. Therefore an unperturbed oscillatory signal in time domain corresponds to a delta function at the center frequency in frequency space.

2.4.1 Overview of phase noise

Following Ref.[9], a real radiation field such as a laser beam undergoes random phase (and amplitude) fluctuations. They can be due to mechanical or thermal fluctuations or of quantum mechanical origin. This is from spontaneous emission of the gain medium into modes of the resonator [8]. As a random process it is not coherent to the original field and causes

---

[6]The formula for the dipole potential and the radial trapping frequency are now slightly modified and can be found in Ref.[45]
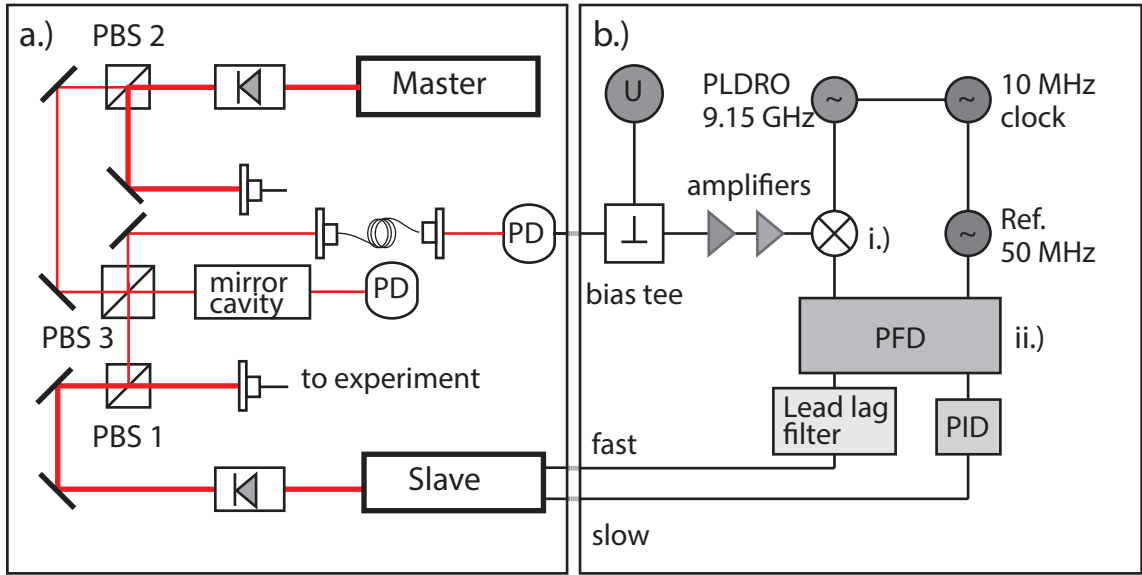
Fig. 2.9: Raman Setup for the stabilization of the phase (frequency) difference between both lasers. The phase of the 'slave' laser is stabilized to the one of the 'master' laser in the optical phase lock loop (OPLL).
a.) Generation of the optical beat signal b.)Downconversion of beat signal (i.)) and generation of error signal (ii.)

phase fluctuations, for instance. The monochromatic radiation field with frequency ω_0 can be thus written as:

$$E(t) = \text{Re}(e^{i(\omega_0 t + \phi(t))}), \tag{2.36}$$

where $\phi(t)$ indicates the phase fluctuations. Phase noise decreases the power at the central, carrier frequency of a pure sine wave, because it spreads the ideal delta function. Close to the carrier the decay of the wings is dominated by $\frac{1}{f}$ noise and far away by thermal noise. Therefore parts of the power are stored in 'noise'powers [6]. It can be measured by recording a power spectral density (PSD) spectrum. The PSD describes the portion of power stored in a certain frequency interval. (Sec. 3.4)[7].

2.4.2 Setup of the Raman OPLL

For coherent Raman transitions on the sidebands between two groundstates with a small frequency spacing, the difference frequency of the Raman lasers has to precisely match the hyperfine energy splitting. Thus, it is necessary to stabilize the phase of one Raman ('slave') laser with respect to the second Raman('master') laser running freely. This is accomplished by means of an optical phase lock loop (OPLL). In an OPLL the phase of a beat signal between both lasers is compared with the phase of a reference oscillator and the error signal is fed back to the 'slave' laser.

The setup for the Raman lasers as it is pictured schematically in Fig.2.9 consists of the generation of the optical beat note on the left hand side (a.) and the circuit for the OPLL on the right (b.). The lasers are temperature controlled interference filter lasers (IFL) which have been built by Ricardo Gomez. In order to avoid any backreflections of light into the lasers the outcoupled laser light from master and slave laser passes an optical isolator [46].

---

[7]The exact expression of the PSD can be found in Sec.3.4, since the whole chapter is denoted to phase noise

For the OPLL we only need a fraction of the total laser power. Thus, most of it will be used for driving the Raman transitions. Therefore, the beam is splitted in a polarizing beam splitter (PBS). By an additional $\frac{\lambda}{2}$ plate each the relative powers are controlled. In the third PBS both beams are overlapped. In order to check single mode operation a fraction of the beat note is sent to a mirror cavity for monitoring the laser modes. The other part serves as the input signal of the OPLL. The corresponding intensity of the beat signal can be calculated by writing the field of a single mode laser as $E(t) = E_0 cos(\omega t + \phi)$. For the intensity it follows:

$$I(t) = \frac{c\varepsilon_0}{2} \left(E_{master}(t) + E_{slave}(t) \right)^2 \tag{2.37}$$

Using $2\cos(\alpha)\cos(\beta) = \cos(\alpha - \beta) + \cos(\alpha + \beta)$ and neglecting the sum term (Bandwidth of photodiode is $10\,\mathrm{GHz}$) one obtains:

$$I = \frac{c\varepsilon_0}{2} (E_0^{master} E_0^{slave} \cos(\Delta\omega t + \Delta\phi)), \tag{2.38}$$

where $\Delta\omega = \omega_{master} - \omega_{slave}$ and $\Delta\phi = \phi_{master} - \phi_{slave}$.

2.4.3 Optical phase lock loop (OPLL)

The optical beat signal sent to the OPLL is first fibre coupled to ensure a good overlap of both beams. The optical beat note is converted into an electrical, containing only the frequency difference of 9.2 GHz between the Raman lasers by a fast photodiode. Referring to Fig.2.9, the bias tee removes any DC offset from the beat signal. As illustrated in Fig.2.4.2 this frequency is mixed down to 50 MHz [47]. Accordingly the beat signal at 9.2 GHz is mixed with a signal at 9.15 GHz from a Phase Locked Dielectric Resonator Oscillator (PLDRO). It is locked to a 10 MHz ^{87}Rb clock. The down converted signal at 50 MHz is compared with a reference signal from a Marconi signal generator in a phase frequency discriminator (PFD). The PFD generates an error signal Ξ proportional to the phase (frequency) difference between the down converted beat note and the reference [47].

$$\Xi \propto sin(\Delta\phi) \tag{2.39}$$

The errorsignal is used to stabilize the frequency of the slave laser and is passed back in two channels. On the one hand the slow feedback with a PID control to the 'slave' laser compensates mechanical vibrations of thermal drifts, for instance. On the other hand the other feedback loop compensates for fast phase and frequency fluctuations [47]. In order to maximize the total power stored in the carrier the laser diode current is controlled by means of a Lead-Lag filter. It increases the feedback bandwidth of the OPLL [48] [47]. The corresponding circuit diagram with the choice of the optimal parameters for our setup can be found in the appendix.

2.4.4 Characterisation of OPLL

In order to determine the functionality of the OPLL one has to determine the total power stored in the carrier and the phase stability with respect to time.
Spectrum of OPLL
For a first characterization the downconverted signal at 50 MHz has been split before entering the PFD and an intensity spectrum around this center frequency recorder. The beat signal was recorded with different spans and resolution bandwidths and the data stitched together in Matlab. We obtained the spectrum as it is shown in Fig. 2.10.[8] The amplitude

---

[8]The corresponding program has been written from my collegue, Ricardo Gomez, who was responsible for this project when I started my thesis.
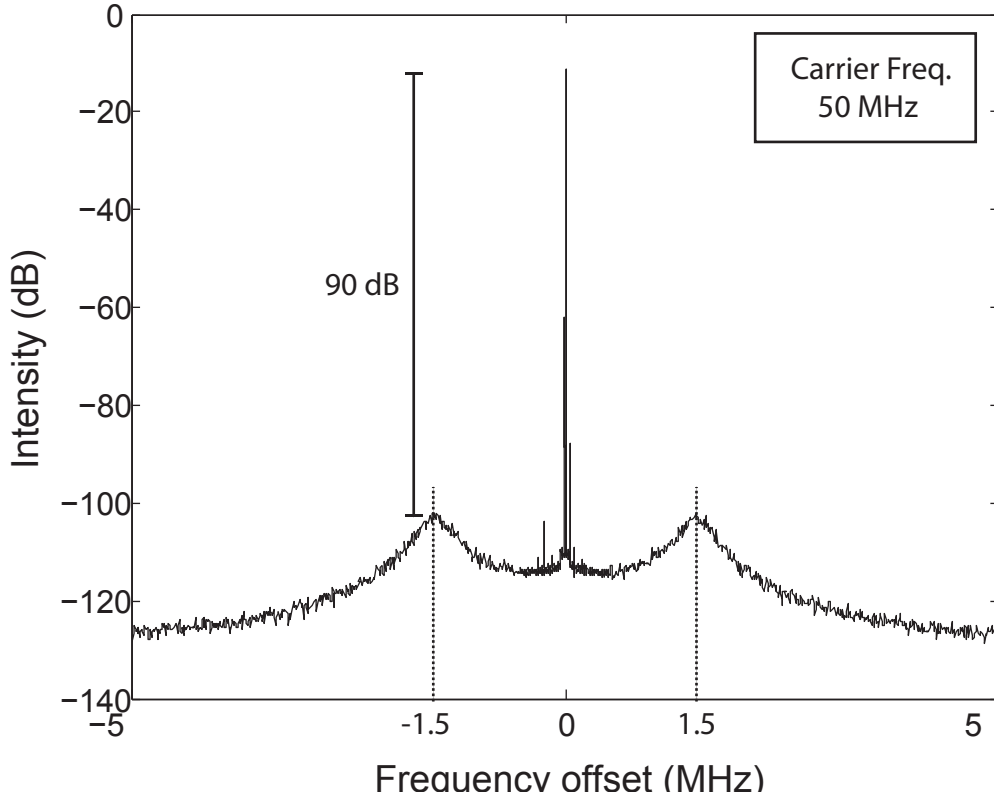
Fig. 2.10: Spectrum of the signal of the OPLL. The x-axis shows the offset from the central (carrier) frequency of 50MHz. The amplitude ration between the carrier and the servo bumps is at 90 dB. The characteristic peaks, called servo bumps, are at 1.5 MHz. They determine the working range of the feedback loop and arise from phase differences that they are not compensated but enhanced by the PFD [47].

of the signal over noise at the carrier frequency at 50 MHz is around 90 dB. The additional peaks, which are symmetrically at ± 1.5 MHz distance from the carrier originate from the case that the phase difference recorded in the PFD is not compensated any more. The phase difference is rather enhanced now and thus sets the limit for the bandwidth of the feedback loop [47]. For this measurement the power on the photodiode was 3.5 mW.

Relative power below the peak

The relative fraction of the total power $P_{rel.}$ stored below the carrier has been calculated by:

$$P_{rel.} = 1 - \frac{P_{noise}}{P_{peak}} \tag{2.40}$$

By dividing the small value of the noise with the comparably high value of the power stored in the peak, one is less sensitive to small changes in the amplitude of the peaks. . The power P_{noise} which is stored outside the carrier is calculated by integrating the area below. However the power in the peak is directly calculated from the maximum value in a small interval. This interval is determined by the width of the curve in the corresponding window of the resolution bandwidth around the carrier. Regarding an estimation of the relative error of the stored power the main contribution is an uncertainty in the determination of the peak

value since it is several orders of magnitude higher than the power loss due to noise. The amplitude of a peak is determined with an accuracy up to ± 0.23 dBm. (c.f datasheet of the Agilent N9020A spectrum analyzer). Consequently, the changes in the calculation of the power are at 0.01%. The maximum value of the peak should be independent from the resolution bandwidth (RBW) of the spectrum analyzer. Referring to Tab. 2.1 this could be verified by measureing the maximum for a small and a big RBW respectively. The difference corresponds to the error of the analyzer. According to Tab.2.1 the maximum is

RBW (Hz)	Peak Value (dBm)
1	-11.51
2000	-11.28
Difference: 0.23 dBm	

Tab. 2.1: Comparison of peak for two different bandwidths

indeed independent from the RBW and reproduces the uncertainty in determining the peak amplitude. The calculation of the fraction of the total power below the carrier yields then:

$$P_{rel.} = (99.91 \pm 0.01)\% \tag{2.41}$$

In a second measurement the power on the fast photodiode was 155μW. The same calculation yielded a value of $P_{rel.} = (98.95 \pm 0.01)$. Referring to this the accumulated power below the carrier does not change significantly with different powers of the beat signal recorded by the fast photodiode. The fractional amount of the total power below the carrier depends on the stability of the phase difference between both lasers, i.e. maintaining a minimal error signal at the output of the feedback loop. In order to characterize the OPLL further and to verify the result from Eq.2.41 I measured the RMS phase noise of the OPLL by means of a quadrature measurement.

2.5 Phase Noise by a Quadrature Measurement

2.5.1 Experimental realization

In order to perform the quadrature measurement both the down converted beat signal at 50 MHz containing the phase noise and a reference signal provided by a Marconi 2032 signal generator at 50 MHz(Splitters from Mini Circuits; ZFSC-2-1-S+ (5-500MHz) and ZSC-2-2+(0.02-60 MHz) respectively) are splitted. The addition of a phase delay of $\frac{\pi}{2}$ to generate the quadrature component corresponds to a length L$= \frac{1}{4}\frac{c}{\nu}$, where ν denotes the frequency of the down converted beat signal. Thus the addition of a BNC cable with a length of 1.48 m led to the phase delay. The in-phase and the quadrature part are mixed each with the reference signal, yielding:

$$I(t) \propto \sin(\omega t + \delta\phi(t)) \cdot \sin(\omega t) = \frac{1}{2}\cos(\delta\phi(t)) \tag{2.42}$$

$$Q(t) \propto \cos(\omega t + \delta\phi(t)) \cdot \sin(\omega t) = \frac{1}{2}\sin(\delta\phi(t), \tag{2.43}$$

where the sum term is lowpass filtered [9]. A quadrature measurement is a method to record temporal fluctuations such as phase noise. For this purpose an arbitrary signal is split into

---

[9]Mixers: Mini-Circuits Type: ZFM-3+ (0.04-400 MHz) , Lowpass filter: Mini-Circuits Type: SLP-30+,50 Ω,DC-32 MHz for I(t) and BLP-10.7+,50Ω,DC-11 MHz
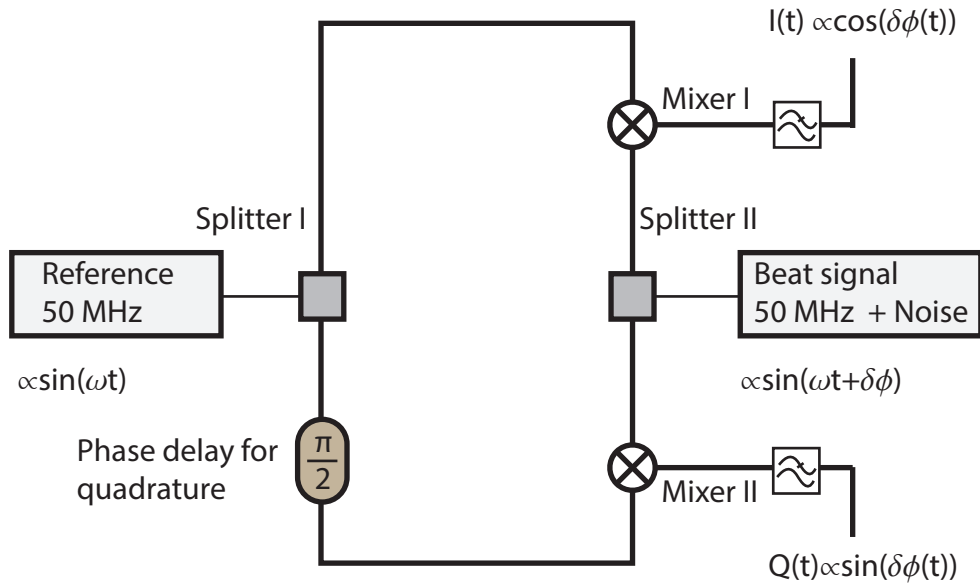
Fig. 2.11: Schematic draft of the experimental setup for the quadrature measurement. The beat signal is split into two arms. For the creation of the quadrature component an additional phase delay of ideally $\frac{\pi}{2}$ is added. Each arm is then mixed with a reference signal, forming the In-phase component $I(t) \propto \cos(\delta\phi(t))$ and the quadrature component $Q(t) \propto \sin(\delta\phi(t))$. Lowpass filters suppress the sum term.
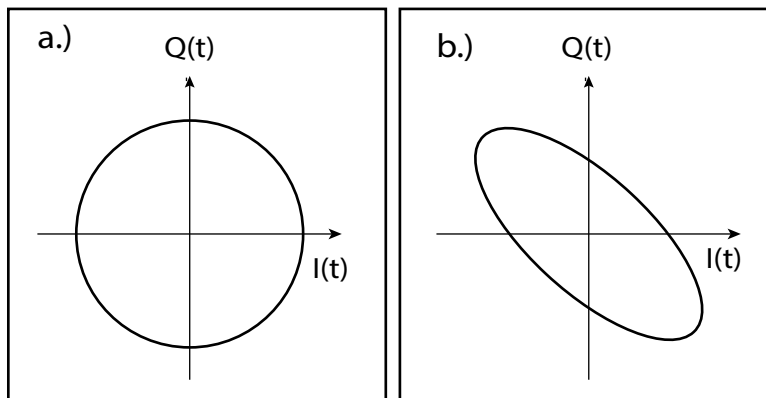

Fig. 2.12: Demonstration of the change of the shape for a deviation of the relative phase difference of $\frac{\pi}{2}$ (a.)). b.) In this case there is a deviation of $\frac{\pi}{4}$ from the perfect phase delay, yielding an ellipse.

two parts. One part is not changed on its way to the detection electronics and is called the in-phase component or abbreviated $I(t)$. The other part is modified such that one adds an additional phase delay of ideally $\frac{\pi}{2}$. As it is illustrated in Fig.2.11 one can achieve that by lengthening the path length between source and detector. It is called the quadrature component $Q(t)$. Thus the signals are equal up to a relative phase difference of $\frac{\pi}{2}$.

Furthermore the temporal evolution of the physical quantity under observation can be traced when the quadrature signals are plotted simultaneously(c.f Fig.2.13. When $Q(t)$ is drawn against $I(t)$, a noiseless signal corresponds to a point on a circle with radius
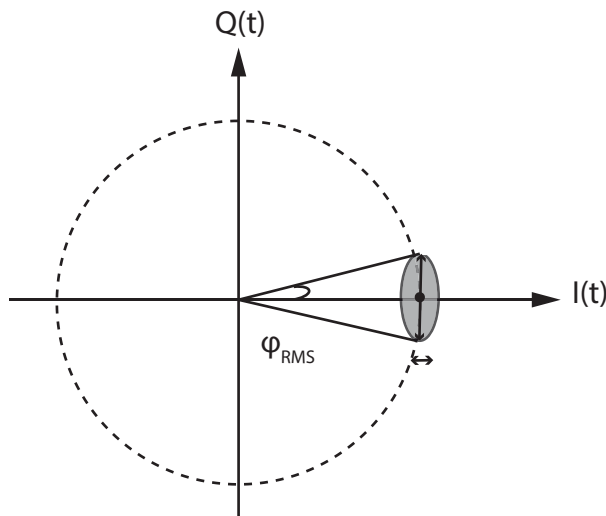
Fig. 2.13: a.) shows a sketch of a quadrature signal with noise in the I(t) and Q(t) branch as it was adjusted for measurement

$r = \sqrt{|\text{I(t)}|^2 + |\text{Q(t)}|^2}$. In case the relative phase difference deviates from $\frac{\pi}{2}$ the overall shape becomes elliptical as it is illustrated in Fig.2.12 for the case of an deviation of $\frac{\pi}{4}$. Fig. 2.12 a.) images the ideal case. For instance, these deviations can occur by mechanical instabilities of the involved components or different cable lengths which lead to an additional delay. However, a signal like the beat note between the Raman lasers contains noise which broadens the point both in direction of I(t) and Q(t), like it is illustrated in Fig.2.13. It is convenient to measure at a point where the amplitude of Q(t)(I(t)) is ideally zero and the other maximal (in a unit circle 1) such that one is on-axis. Furthermore the contribution from noise is much smaller than the maximal value of the amplitude of I(t)(Q(t)). Therefore the fluctuations of the quadrature component on axis can be neclected. Additionally the remaining amplitude of the perpendicular component is purely governed by the (phase) noise of the signals because it fluctuates around zero. Hence the RMS value of the phase noise can be obtained directly. From Fig. 2.13 one infers the following expression for the RMS-value of the (phase) noise with the time averaged amplitude values of Q(t) and I(t) for small angles.[10]

$$\phi_{\text{RMS}} \approx \left(\frac{\langle \text{Q(t)} \rangle}{\langle 2\text{I(t)} \rangle} \right) \tag{2.44}$$

Moreover, a spectral analysis of the electric field in the presence of noise leads to a useful expression, which connects the fraction of total power below a signal with the RMS value of the phase noise. [11]

$$P_{\text{carrier}} \propto e^{\langle \phi_{\text{RMS}} \rangle^2} \tag{2.45}$$

Comparing the results from the quadrature measurement with the ones from the calculation of the area below the curve of the signal from the OPLL offers the possibility to verify the results by independent measurements.

---

[10]Since both components possess the same source from which the noise is measured by this method, the magnitude of fluctuations for Q(t)and I(t) respectively should be akin. Therefore it is a valid approach to infer the (phase) RMS noise by means of Eg. 2.44.

[11]A more detailed derivation of this relationship can be found in Appendix. B which follows Ref. [49]

2.5.2 Result

I measured the RMS values of the amplitudes of Q(t) and I(t) in the way like described above in units of mV on an oscilloscope. With an amplitude of $\langle I(t) \rangle = 150$mV and $\langle Q(t) \rangle = (10 \pm 0.5)$ mV, a phase noise of was measured.

$$\phi_{\text{rms}} = (0.033 \pm 0.001) \, \text{rad} \tag{2.46}$$

Using Eg.2.45 the power stored in the carrier could be calculated It yields:

$$P_{\text{carrier}}^{\text{Quad.}} = (99.89 \pm 0.01) \, \% \tag{2.47}$$

This value is in good accordance with the value from Eq.2.41. These characterization measurements demonstrate that the frequency difference between the Raman master and slave laser is well stabilized. Less than 0.5% of the total power are not concentrated below the carrier.

2.6 Experimental Setup

With a setup of two Raman lasers whose frequency difference is stabilized by an OPLL an important prerequisite for the implementation of the Raman setup is fulfilled. In Fig.2.14 the experimental setup with the components needed for the three dimensional ground state and its detection is schematically illustrated. The following represents a short overview about the components. Detailed information can be found in the given references and references therein.

- **Vacuum and glass cell**
  Collisions between the atoms and particles of the thermal background gas increase the possibility to heat the atoms out of the optical lattce [38]. Therefore experiments with cold atoms in optical lattices are performed in ultra high vacuum. The center of the trapping region, e.g MOT beams and optical lattice, is located within the central position of a glass cell which provides almost full optical access and simplifies alignment of the imaging optics [29].

- **Magneto optical trap (MOT)**
  The atoms are precooled in a magneto optical trap (MOT) by three dimensional Doppler cooling [29, 38] . The application of a magnetic field gradient corresponds to a postion dependent repulsive force which traps the atoms in the center of the optical molasses [35]. As it is also shown in Fig.2.14 the xy plane of the MOT owns a relative angle of $45°$ to the axis of the otical lattice. The third MOT beam, the z-beam, is sent from top.

- **Optical lattice** The trap is generated by a Ti:Sa laser at 865.9 nm, whose light is splitted into two arms called dipole trap one (DT1) and dipole trap two(DT2). The quantization axis is along the direction of the counterpropagating beams DT1 and DT2 forming the optical lattice. DT2 is linearly polarized and DT1 a linear superposition of a purely σ^+ and σ^- polarized beams. This is generated by direct polarization synthesis [50]. Operating at this wavelength leads to a state dependent optical lattice (2.1.3). As stated before the two basis states for manipulation of the atoms are the hyperfine states $|\text{F=4, m}_\text{F}\text{=4}\rangle \equiv |\uparrow\rangle$ and $|\text{F=3, m}_\text{F}\text{=3}\rangle \equiv |\downarrow\rangle$.

- **Doughnut beam**
  A standing wave optical lattice provides a strong confinement in the axial direction,
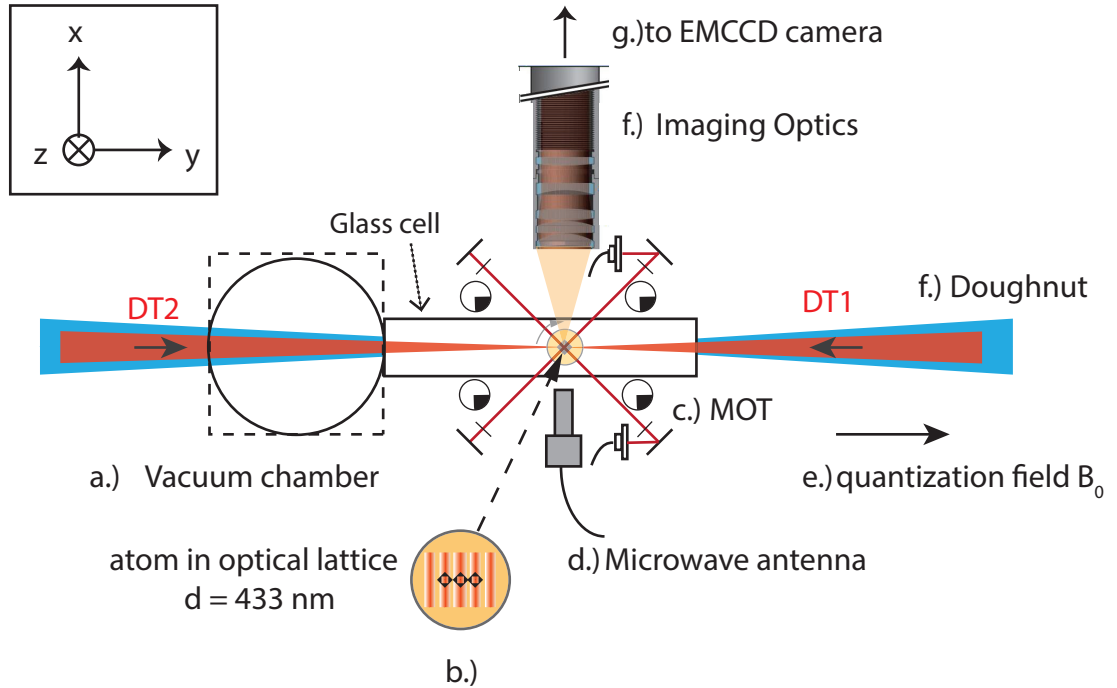
Fig. 2.14: Experimental apparatus for cooling and trapping the cesium atoms. For simplicity only the main components are shown. a.) Vaccum chamber with attached glass cell b.) State dependent optical lattice by dipole trap arm one (DT1) and DT2 respectively c.) Magneto optical trap (MOT) d.) Microwave antenna e.) Quantization axis by guiding field f.) Imaging optics including objective with NA=0.29 [29]. g.) EMCCD camera for fluorescence detection. Further references in text.

enabling the resolution of sidebands. However for the 3D ground state the sidebands have to be resolvable in radial direction as well and the atoms in the Lamb-Dicke Regime [40]. Thus additional radial confinement is necessary. See for Sec.2.3.2 and references therein.

- **Imaging system and EMCCD detector**
  For imaging the fluorescence light from the atoms is collected by a high numerical aperture (NA) objective with NA=0.29 [29]. The images are taken by an EMCCD (Electron Multiplying Charge Coupled Device) camera. Further information can be found in Ref. [29, 38],[26].

- **State preparation and detection**
  An external guiding magnetic field with $B_0 \equiv B^{quant.}$ lifts the degeneracy by the Zeeman effect and defined the quantization axis. The atoms are initialized in the $|\uparrow\rangle$ state by optical pumping with a σ^+ polarized laser beam which is resonant to the F= 4 →F'= 4 transition($62^P_{1/2}$ state). Atoms which decay by spontaneous emission to the F= 3 state are brought back to the pumping cycle by an equally polarized re-pumper. This one is resonant to the $F = 3 \rightarrow F' = 4$ transition. The $|\uparrow\rangle$ state is a dark state. The atomic states are detected by means of the 'push-out' technique. [26, 38]

- **Microwaves**
  The full control over the qubit states is completed by manipulating the internal states of the atoms by microwave radiation pulses. The atoms are adressed with single site
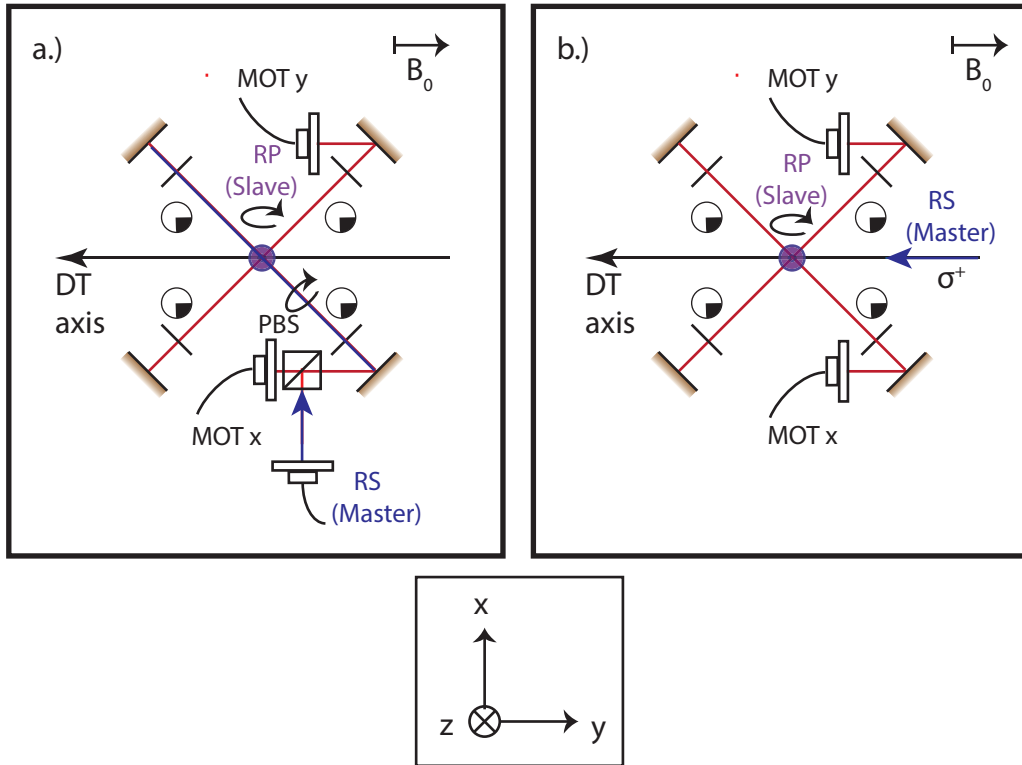
Fig. 2.15: Comparison of the two configurations. For the final cooling the b.) was used.

resolution. For instance, a π pulse transfers the atom from $|\uparrow\rangle$ to $|\downarrow\rangle$. [38, 26]

2.6.1 Configurations for cooling

The atoms are precooled in the MOT and then transferred into the optical lattice [26] which is overlapped with the doughnut beam (c.f 2.8). By optical pumping the atoms are prepared in the initial state $|\uparrow\rangle$ for the cooling process. In a first attempt toward cooling the Raman lasers are both circularily polarized at the position of the atoms and overlapped with the the z-axis (Raman pump laser) and the MOT x-axis (Raman Stokes laser) in retroreflection. For the second configuration as shown in Fig.2.15 b.) the polarization of the Raman stokes(master) has been changed to a purely σ^+ polarized beam. Additionally it is now overlapped with the dipole trap axis.

Configuration of k-Vectors

For cooling the atoms have to undergo a momentum kick in the radial direction, which is in opposite direction to their velocity [35]. The corresponding momentum kick is shown for both configurations in Fig.2.16 a.) and b.) respectively. For simplicity the retroreflected beam is not represented in Fig.2.16 a.) and only two of the four momentum vectors Δk_i are shown. The others would generate a reflection of the figure with the xy plane. Referring to Fig. 2.14 the doughnut beam is overlapped with the dipole trap. It was measured that the doughnut has a slight ellipticity (5 10%) which is tilted by $45°$ to the momentum kick Δk in the transversal direction. Therefore, the momentum kick (c.f Fig.2.16 b.)) couples both transversal directions.
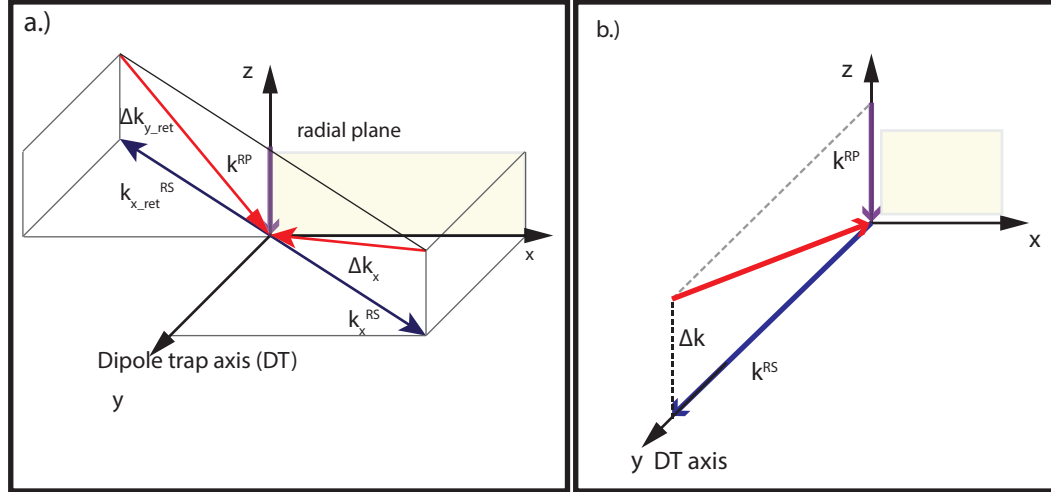
Fig. 2.16: Illustration of the momentum kick for both configurations. a.) shows the first attempt. b.) Used Configuration for cooling into the ground state

Hyperfine prefactors

In the presence of a hyperfine splitting the Rabi frequencies have to be modified to take into account the different coupling strengths of the hyperfine states. These relative weights are given by the Clebsch-Gordan-coefficients C_{ij}. Therefore the new Rabi frequency can be written as:

$$\Omega_{|F,m_F\rangle \to |F',m_{F'}\rangle} = \langle F,m_F| \hat{e}\varepsilon_0 E_0 |F',m_{F'}\rangle = C_{ij} \langle J| \hat{e}\varepsilon_0 E_0 |J'\rangle, \qquad (2.48)$$

where the indices ij correspond to i= $|F,m_F\rangle$ and j= $|F',m_{F'}\rangle$ The coefficients relevant for both configurations are listed in Tab.2.2.

Label	Transition	C_{ij}
$C_{44\leftrightarrow 4'4'}$	$|F=4,m_F=4\rangle \leftrightarrow |F'=4,m_{F'}=4\rangle : \pi$	$\sqrt{\frac{7}{30}}$
$C_{33\leftrightarrow 4'3'}$	$|F=3,m_F=3\rangle \leftrightarrow |F'=4,m_{F'}=3\rangle : \pi$	$\sqrt{\frac{5}{96}}$
$C_{33\leftrightarrow 3'3'}$	$|F=3,m_F=3\rangle \leftrightarrow |F'=3,m_{F'}=3\rangle : \pi$	$\sqrt{\frac{9}{32}}$
$C_{44\leftrightarrow 4'3'}$	$|F=4,m_F=4\rangle \leftrightarrow |F'=4,m_{F'}=3\rangle : \sigma$	$\sqrt{\frac{7}{120}}$
$C_{44\leftrightarrow 3'3'}$	$|F=4,m_F=4\rangle \leftrightarrow |F'=3,m_{F'}=3\rangle : \sigma$	$\sqrt{\frac{7}{72}}$
$C_{33\leftrightarrow 4'4'}$	$|F=3,m_F=3\rangle \leftrightarrow |F'=4,m_{F'}=4\rangle : \sigma^+$	$\sqrt{\frac{5}{24}}$

Tab. 2.2: Values of the relevant Clebsch Gordan coefficients for employment of the Raman beams

Configuration I

Both Raman lasers are circularly polarized which means that according to the relative position to the quantization field both could in principle drive σ^+, σ^- and π transitions. The
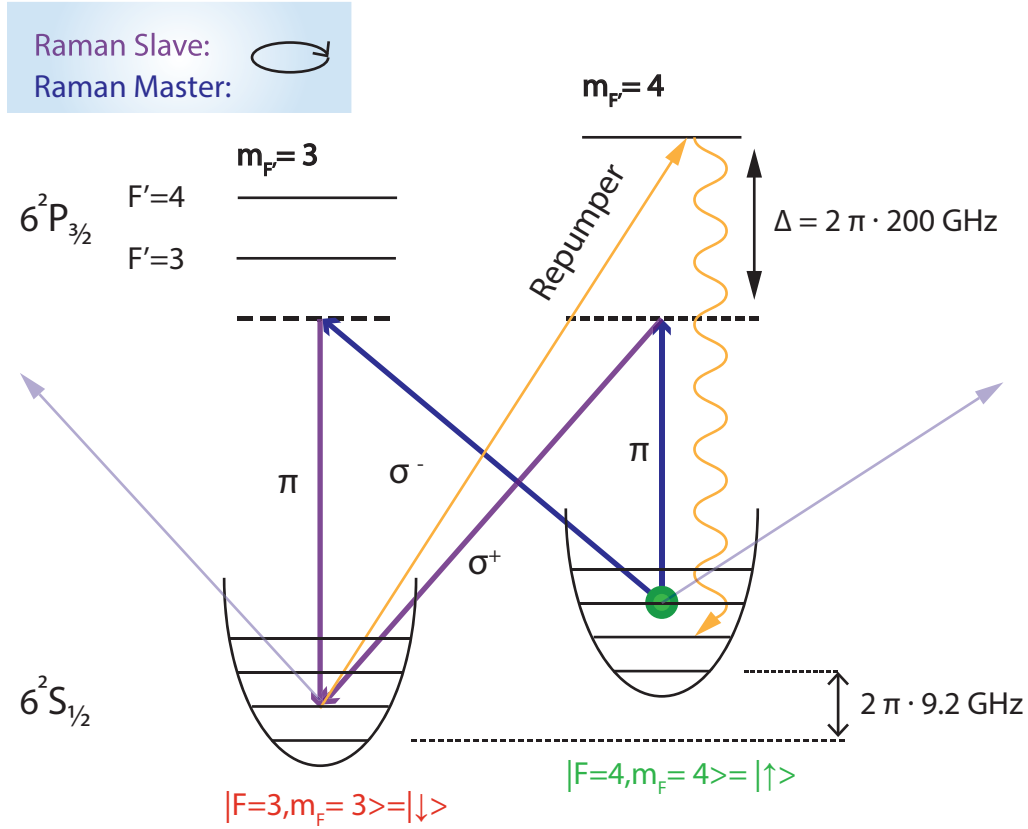
Fig. 2.17: Illustration of the Raman sideband cooling in the first attempt. The RP beam is tuned to the first blue sideband. The Raman pump (RP) and the Raman stokes (RS) laser are detuned by Δ from the D2 line of cesium. The atom, initially in $|\uparrow, n+1\rangle$ is pumped to the intermediate state. Then stimulated emission by the RS beam transfers the atom into $|\downarrow, n\rangle$ A repumper transfers the atoms to the $|\uparrow, n\rangle$ state.

power is equally distributed over the different polarizations.

$$P_{\mathbf{all}} = \frac{1}{3}\left(P_{\sigma^+} + P_{\sigma^-} + P_\pi\right) \tag{2.49}$$

Due to the selection rules from quantum mechanics only the π and σ^- polarized fraction of light from the Raman pump(RP) and the π and σ^+ fractions from the Raman stokes(RS) laser can be exploited for Raman sideband cooling. The states $|\uparrow, n+1\rangle$ and $|\downarrow, n\rangle$ are coupled by a combination of either $\pi\sigma^+$ or $\sigma^-\pi$ of the Raman lasers as it is illustrated in Fig.2.17. The atom is prepared by optical pumping in $|\uparrow\rangle$ and the Raman pump laser is tuned to the first blue sideband. The cooling cycle is closed by a repumper to $|\text{F'} = 4, \text{m}_{\text{F'}} = 4\rangle$ and spontaneous emission.

This configuration of the laser's polarizations allows to use $\frac{2}{3}$ of the total power of the Raman beams. For the resulting coupling strength all contributions in the hyperfine structure have to be considered. Referring to Fig.2.17 the σ^- polarized light component from the Raman pump laser can either excite the atom to an intermediate state detuned from the $|\text{F'} = 4, \text{m}_{\text{F'}} = 3\rangle$ or to the $|\text{F'} = 3, \text{m}_{\text{F'}} = 3\rangle$ state with coupling strengths depending on the Clebsch-Gordan coefficients. The corresponding hyperfine prefactors are $\sqrt{\frac{7}{120}}$ and $\sqrt{\frac{7}{72}}$ respectively (c.f. Tab. 2.2,[37]).
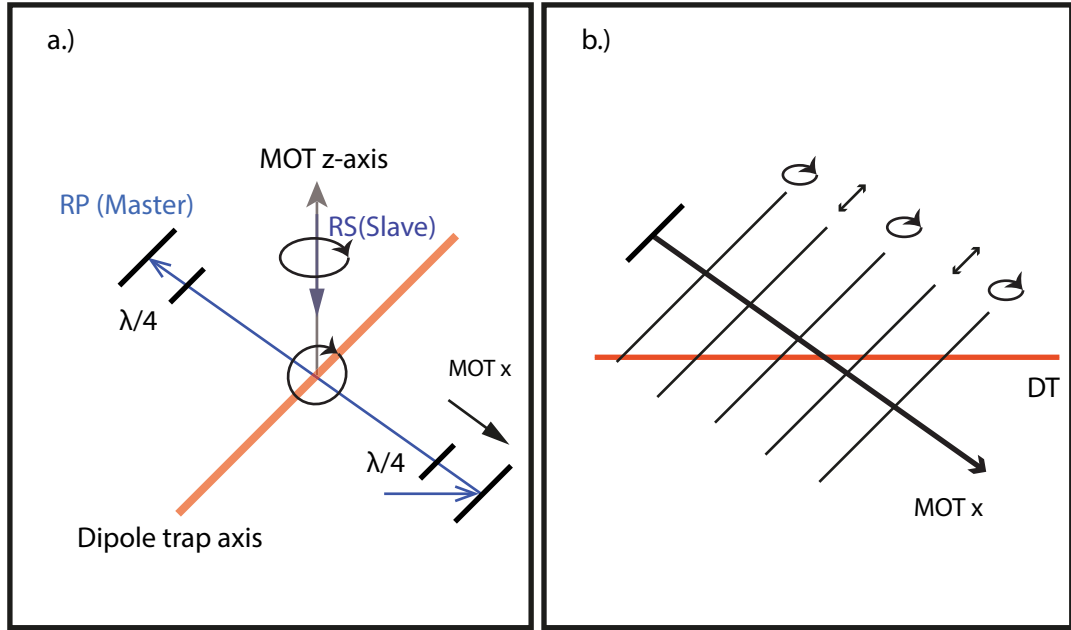
Fig. 2.18: Illustration of the polarization gradient.
a.) shows the direction of the both circularily polarized Raman lasers. b.) displays the resulting spatial gradient of polarization which leads to varying ones at different lattice sites.

With respect to all contributing transitions and corresponding hyperfine prefactors both processes possess the same coupling strength and contribute equally to the cooling:

$$\pi\sigma^+ :$$

$$C_{44\rightarrow4'4'} \cdot C_{4'4'\rightarrow33} : \frac{\sqrt{7}}{12}$$

$$\sigma\ \pi :$$

$$C_{44\rightarrow4'3'} \cdot C_{4'3'\rightarrow33} + C_{44\rightarrow3'3'} \cdot C_{3'3'\rightarrow33} = \frac{\sqrt{7}}{12}$$

Problems of configuration I

It was not possible to resolve longitudinal or transversal sidebands with the Raman lasers by that beam configuration . The following things have been tried to resolve sidebands:

- Raman spectroscopy with $\Delta = 50\,\text{GHz}$
  Observation of spontaneous Raman transitions from at least one laser

- Change of the detuning to $\Delta = 200\,\text{GHz}$
  The sidebands were still not visible. If they were not visible due to power broadening they should appear, when the beam power is changed

- Decrease of the powers from both Raman lasers in steps from mW to μW range.

One reason could be the alignment of the Raman lasers in retroreflection configuration(c.f.Fig.2.15 a.)) and the circular polarization of the beams at the position of the atoms.

In Fig.2.18 a.) the geometrical configuration and the circular polarization of the beams is shown. It leads to a polarization gradient along the retroreflected Raman beam (Fig. 2.18 b.)). This results in varying polarizations for atoms in different lattice sites. Hence, the Rabi
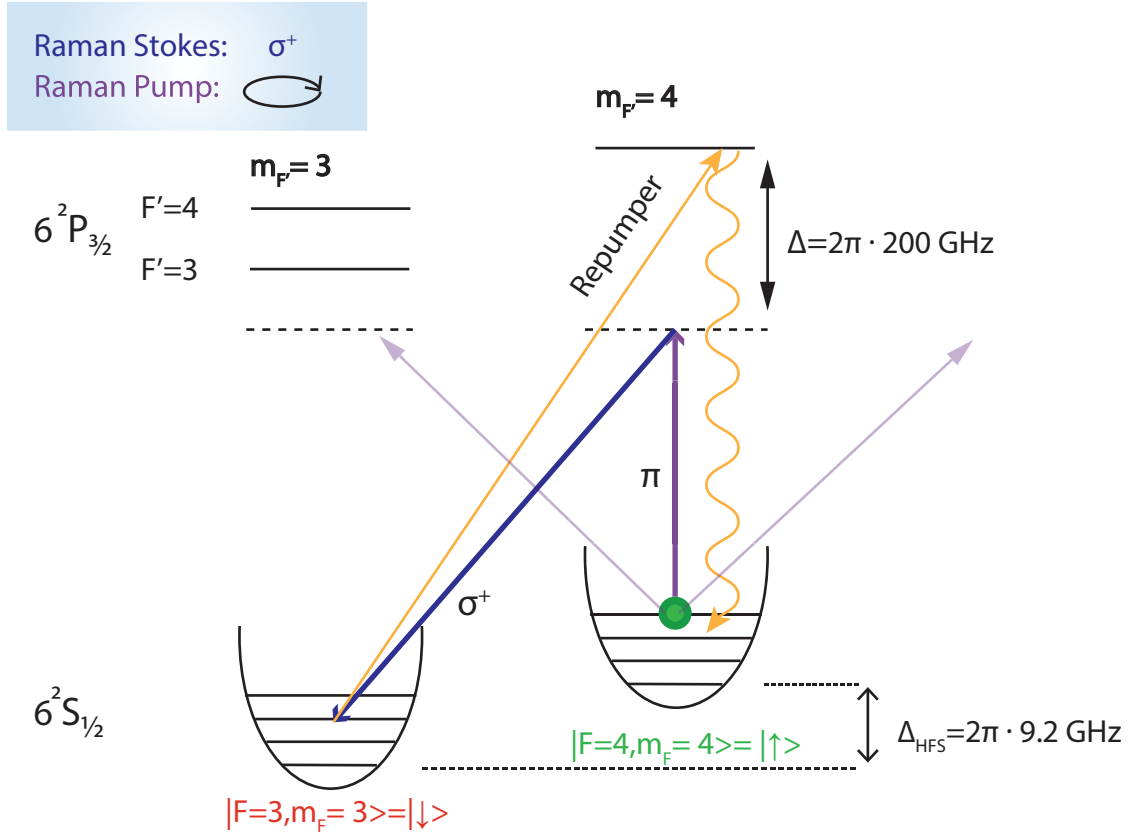
Fig. 2.19: Illustration of the configuration of used transitions for our Raman sideband cooling
scheme.

frequency depends on the position of the atoms. This, for instance, could explain why it
was not possible to record Raman Rabi oscillations. Theoretically one should observe still
sidebands. However, these were probably not visible due to decoherence.

Scheme II

After these attempts is has been decided by the group to change the geometry of the Raman
beams. As it is illustrated in Fig.2.15 the Raman stokes (master) laser is overlapped with
the axis of the dipole trap and purely σ^+ polarized. The choice of this geometry avoids
a polarization gradient and as shown in Fig.2.19 allows to use only one combination for
driving Raman transitions. The Raman pump laser remains circularily polarized and can
therefore drive σ^+, σ $and \pi$ transitions. Accordingly the combination from a π transition
followed by a σ^+ transition induces Raman transitons. Initially the atom is prepared in the
$|\uparrow\rangle$ state by optical pumping. The Raman transition remains detuned by 200 GHz as before.
As it is also displayed schematically in Fig.2.19 the atom is pumped to the intermediate state
by the fraction of the Raman pump light which is π polarized, from which it is transferred
into the $\downarrow$ state by the Raman stokes beam by stimulated emission. Due to the transition on
the blue sideband the motional state number has been lowered by one. The cooling cycle
is closed by a repumper and spontaneous emission to the initial state, but with a motional
number decreased by one. The hyperfine prefactor for the coupling strength is given by:

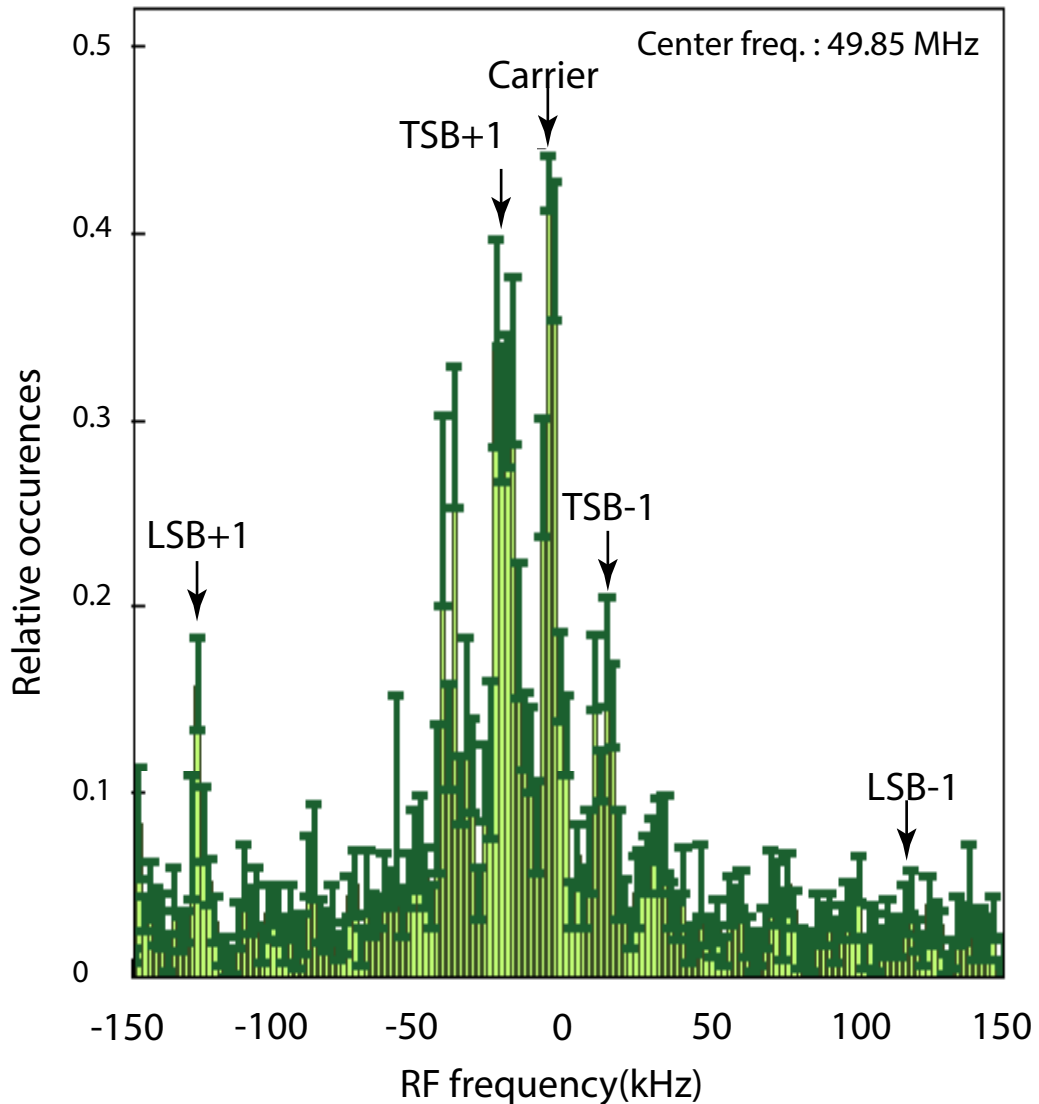$$\pi\sigma^+ = \frac{\sqrt{7}}{12} \tag{2.50}$$

Fig. 2.20: Demonstration of cooling into the motional ground state. The whole spectrum is shown. The transversal sidebands are as expected separated from the carrier frequency at $\pm 49.85\,\text{MHz}$ by $\approx \pm 20\,\text{kHz}$. At 110 kHz from the carrier the first longitudinal heating sidebands appear.[With kind permission by C. Robens]

2.7 Cooling into the ground state

With the second configuration (Fig.2.15 b.) it is possible sidebands apeear. Thus the atoms are cooled. Figure 2.20 reveals the complete result of the measurement. The asymmetry between the number of the relative occurences between the red and blue transversal sideband respectively displayed in Fig.2.20 indicates that a significant fraction of atoms has been tranferred into the motional ground state.
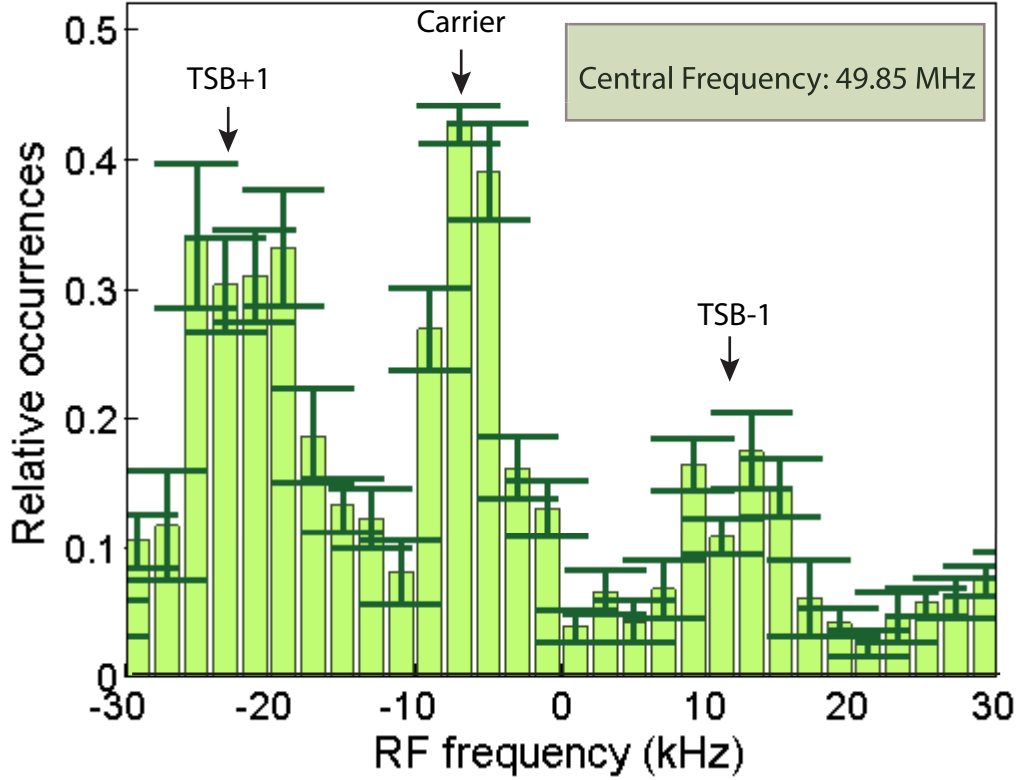
Fig. 2.21: Illustration of the carrier and the first transversal sidebands for a smaller span.
[With kind permission by C. Robens]

Peak	Position	Height	Width
TSB+1	(21.71 ± 1.74)	(0.34 ± 0.03)	(11.19 ± 0.9)
Carrier	(6.32 ± 0.5)	(0.43 ± 0.03)	(6.3 ± 0.5)
TSB-1	(11.74 ± 0.94)	(0.15 ± 0.01)	(12.05 ± 0.96)

Tab. 2.3: Results of the Gaussian Fit to the data

Analysis

Following the calculation presented in Sec.2.2.2, the ratio and thus the probability to be in
the ground state after cooling can be calculated. In order to calcuated the ratio R, the relative
heights of the blue (TSB-1) and red sideband (TSB+1) have to be determined. For better
visualization of that region Fig.2.21 shows the carrier and the first transversal sidebands.
The relative heights of the sidebands are determined by a Gaussian fit [51] to the data, as it
is illustrated in Fig.2.22. The result from the fit is listed in Tab.2.3 This yielded a ratio of
$R = (0.44 \pm 0.05)$ and thus the probability that the atoms have been cooled into the motional
ground state (from the radial sidebands) to be:

$$P_0 = (0.56 \pm 0.01) \qquad (2.51)$$

Accordingly approximately 56 % of the atom are cooled in the radial sidebands.
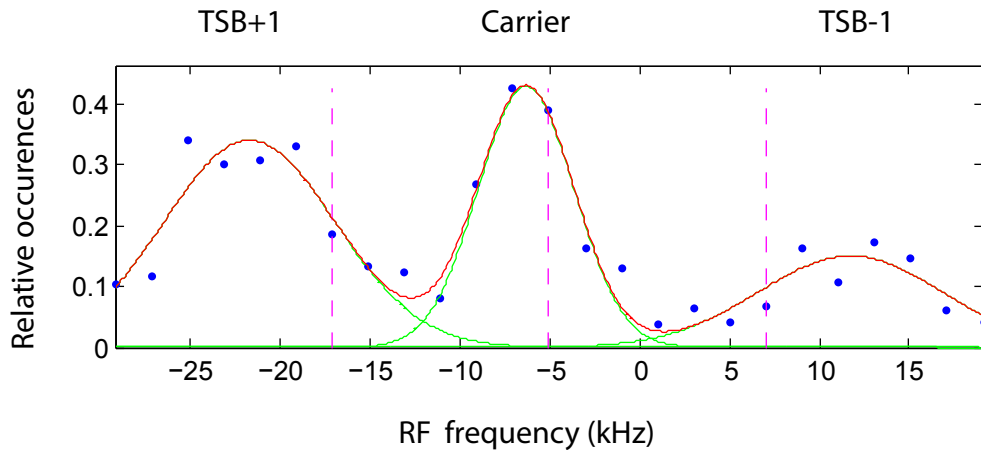
Fig. 2.22: Result of a Gaussian Fit for the carrier and the first transversal sidebands. The corresponding values are listed in Tab.2.3.

2.8 Summary

In this chapter I presented the setup to cool the atoms in the radial plane to reach the motional ground state which is crucial for reproducible atom-atom interactions. The atoms are cooled by employing Raman transitions which are tuned on the first blue sideband transition between the basis states denoted by $|\uparrow\rangle$ and $|\downarrow\rangle$, respectively. In order to drive coherent Raman transitions the phase between both Raman lasers has to be stabilized by using an optical phase lock loop(OPLL). It has been characterized by recording an intensity spectrum and calculated the power stored below the carrier at $50\,\text{MHz}$ by integration to be $(99.91 \pm 0.01)\%$. By an independent measurement of the phase noise in quadratrature configuration I obtained a value of $\phi_{\text{RMS}} = (0.033 \pm 0.001)\,\text{rad}$. I could confirm the value of the power below the carrier. The result is that $(99.89 \pm 0.01)\%$ of the total power are stored below the carrier. This is in good accordance with the result from integration. Thus the phase is well stabilized. In the present setup the Raman transitions are driven by a πtransition to the intermediate state which is followed from a σ^+ transition. With this configuration it is possible to cool atoms into the motional ground state with a probability of $(56 \pm 1)\%$

Combining this with the progress with respect to the position control of single atoms to transport them to the same lattice site enables us now in principle to conduct the Huong-Mandel experiment with massive bosonic particles [18, 19]. Of course this comes along with the great progess in the control and manipulation of the qubit states of the atoms which has been developed over the past years also in our group.

3

Common Mode OpticalPhase Noise of the Optical Lattice

As pointed out in the introduction a good knowledge about the limiting factors, i.e. noise, is also important for the successful conduction of an experiment with reliable results. This is also called the 'errorbudget' of an experimental apparatus. In our experiment several contributions to the 'errorbudget' such as identifying beam pointing instabilities as one source of decoherence [28] or heating of the atoms have been already well studied and characterized [29]. However, the impact of a phase noise induced by the optical lattice, has not been studied yet. The state dependent optical lattice, which consists of two standing wavepotentials denoted by $U_{\sigma+} = U_\uparrow$ and $U_{\sigma-} \approx U_\downarrow$ represents the centerpiece of the experimental apparatus. Hence, it is of importance to find out whether such noise leads to heating of the atoms or a decrease in the single-site resolution. Such a phase noise can either be due to a differential movement or to a common mode movement of the relative phase between the lattice potentials $U_\uparrow$ and $U_\downarrow$. The differential movement can in principle result in an addional relative phase between the atoms which makes them distinguishable although they are in the motional ground state. However, for the clear demonstration of the Huong-Mandel effect with atoms [19] the atoms should be indistinguishable. The common mode optical phase noise corresponds via $\Delta\phi = k \cdot \Delta s$ to a spatial shift. This could lead to uncertainties in the determination positions of the atoms. Since both atoms have to be brought to the same lattice site this phase noise could decrease the fidelity of such a process. In the following I will focus on the examination of the common mode phase noise of the optical lattice. In order to measure the common mode phase noise the two dipole trap beams DT1 and DT2 (c.f Fig.3.1) have to be overlapped. Therefore I assembled an interferometer. In order to minimize additional phase noise from itself the interferometer was built in a small, monolithic cube (Fig. 3.2 a.). In the following both the fast oscillating and slowly drifting contribution will be considered. In Section 3.5 first the power spectral density(PSD) spectrum will be examined, which represents the fractional amount of total power in a certain frequency interval [9]. Regarding the slow drifts (Section 3.6) a possible influence on the position reconstruction of the atoms will be analyzed.

3.1   Experimental Setup

A linearly polarized Titanium-Sapphire laser [Coherent MBR−110,abbrev. TiSa,[38]] with an maximum output power of 2.2 W at 865.9 nm wavelength serves a the source of the state dependent optical lattice. The first polarizing beam splitter (PBS) creates the two arms of the interferometer, denominated in the following with dipole trap arm one(DT1) and dipole
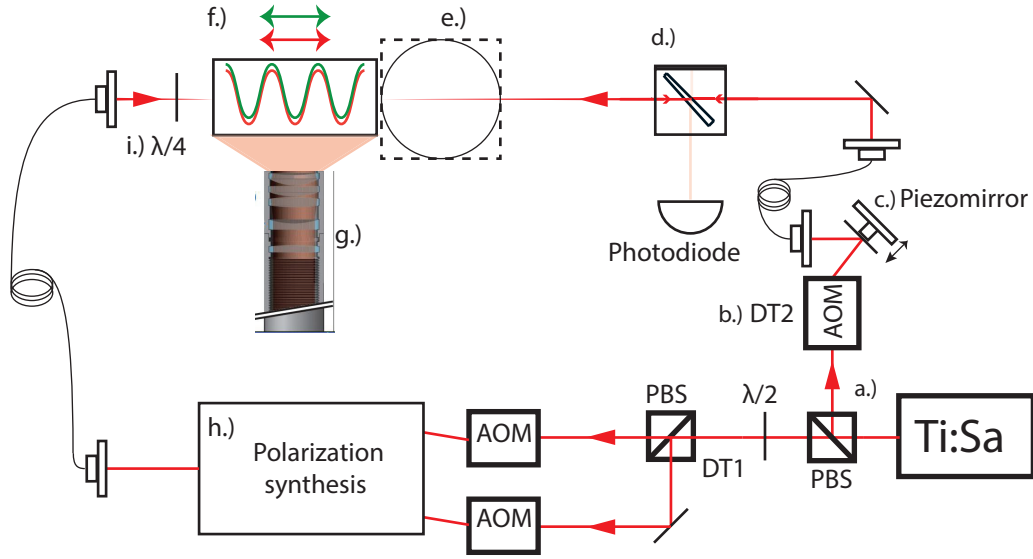
Fig. 3.1: Schematic of the experimental apparatus including the new interferometer to measure the common mode optical phase noise. A PBS splits the light from a titan sapphire laser(Ti:Sa, a.)) into two dipole trap arms (DT1 and DT2). The beam of DT2 is passing an AOM (b.)) for power control. The piezo mirror(c.)) allows to control the relative phase between both arms. At the interferometer (d.)) 10% of the light are picked up to measure the global phase noise. The rest passes the vacuum chamber with attached glass cell (e.) to the formation of the optical lattice (f.). The imaging apparatus collects the fluorescence light for analysis ((g.),[38]). DT1 is split into two arms for the polarization synthesis(h.)) leading to our state dependent optical lattice [50].The linear polarized light is converted into circularily polarized light i.).

trap arm two(DT2). While the acousto optical modulator (AOM) in the beam path of DT2 is only used for intensity stabilization the AOM's in the path of DT1 are also used to adjust the optical phase for the polarization synthesis. Acousto optical modulators for a further control of the laser power and the detuning of the frequency are inserted. The AOMs are driven by a 80 MHz RF source. For the polarization synthesis the light of DT1 is divided again by a second PBS. These are then DT1R and DT1L respectively. It is used to realize state dependent transport [50]. The arm DT1 is linearly polarized and reaches the position of the interferometer after passing the vacuum chamber. The other arm, (DT2) passes first the interferometer and reaches then the glass cell, as it is illustrated in Fig.3.1. There 10% of the light is picked up for the beat signal and the rest is transmitted to the atoms as well (c.f Sec.3.2). These counterpropagating beams then form operating at a 'magic' wavelength of 866 nm the state dependent optical lattic (c.f Chap.2.1.3).

3.2 The Interferometer

As one can also depict from Fig. 3.3 a.) the interferometer is similar to a classical Michelson-Morley interferometer[52]. Two counterpropagating beams, the lattice beams DT1 and DT2, are superimposed using a wedged glass plate. The resulting beat signal provides a direct measurement of the common mode phase noise. Both arms are from the same laser source, the Ti:Sa laser, as illustrated in Fig.3.1. The fields of each contribution are defined

as:

$$\mathbf{E}_{\mathrm{DT1}} = \mathrm{E}_{01} \cdot e^{i(\omega t - \mathrm{k}x_1)}, \tag{3.1}$$

$$\mathbf{E}_{\mathrm{DT2}} = \mathrm{E}_{02} \cdot e^{i(\omega t - \mathrm{k}x_2)}, \tag{3.2}$$

where k is the wavenumber, x_1 and x_2 respectively denotes the total path length to the point where these partial waves are superimposed. The resulting total intensity can be calculated as where $\Delta x = x_2 - x_1$ represents the relative path length difference between both arms of the interferometer [53].

$$\mathbf{I}_{\mathrm{all}} = \mathbf{I}_1 + \mathbf{I}_2 + 2\sqrt{\mathbf{I}_1 \mathbf{I}_2} \cdot \cos(\mathrm{k}\Delta x) \tag{3.3}$$

This result represents the ideal case without any time dependent fluctuations. In our timescales a real measurement device as a spectrum analyzer always detects the temporal mean value of this observables, therefore it measures:

$$\langle \mathbf{I}_{all} \rangle = \langle \mathbf{I}_1 \rangle + \langle \mathbf{I}_2 \rangle + 2\sqrt{\langle \mathbf{I}_1 \rangle \langle \mathbf{I}_2 \rangle} \cdot \langle \cos(\mathrm{k}\Delta x) \rangle \tag{3.4}$$

Changes in the relative pathlength as the common mode movement of our optical lattice correspond via $\Delta \phi = k\Delta x$ to a change in the optical phase. The cosinusodial interference pattern becomes visible when $\Delta \phi \geq 2\pi \quad (\Delta x = \frac{n}{\lambda}, n \in \mathbb{Z})$. When the averaged intensities $\langle \mathbf{I}_1 \rangle$ and $\langle \mathbf{I}_2 \rangle$ are known, one can estimate how well both beams are overlapped from the interference constrast. Thus by measureing and increasing the contrast the overlap can be optimized. For the case of equal intensities values the maximal theoretical contrast has a value of one. The general expression yields [53]:

$$V = \frac{2\sqrt{I_1 I_2}}{I_1 + I_2} \tag{3.5}$$

Experimentally, the contrast can be determined by changing the optical phase $\Delta \phi$ and recording the minimal and maximal intensity of the beat signal.

$$V = \frac{I_{\max} - I_{\min}}{I_{\max} + I_{\min}} \tag{3.6}$$

,where $I_{\max}$ denotes the case of an optical phase such that $\cos(\mathrm{k}\Delta x) = 1$ and $I_{\min}$ for $\cos(\mathrm{k}\Delta x) = -1$ in Eq.3.3 [54]. The contrast takes values between 0 and 1 and this expression also reasons why it is necessary to match the level of both intensities.

3.3 Generation of the Beat Signal

All components of the interferometer are placed in a quadratic, monolithic cube with side-lengths of five centimeters each as it is shown in Fig.3.2 a.). This compact design ensures that the interferometer does not add phase noise by itself. A wedged glass plate serves as a beam splitter as displayed in Fig. 3.2b.) and c.) Referring to Fig. 3.3 a.) the wedged glas (NBK-7) plate has got an antireflection coating(AR) on the side of the arm coming from the atoms. The glass plate is wedged to both interference with the AR coated side. Additionally the wedge is inserted such that the reflection from the mirror does not reach the vacuum chamber, i.e the atoms. For a perpendicular incidence of light to the fixed mirror the wedged glas plate is tilted by $45°$ relatively to the light of DT2. It reflects 10% and transmits 90% of the light. The arm of DT2 with a power P_2 hits the glas plate under an angle of $45°$, is reflected to the fixed mirror and then transmitted back through the glas plate towards a photodiode. The other arm, DT1, is first transmitted due to the antireflection coating and then
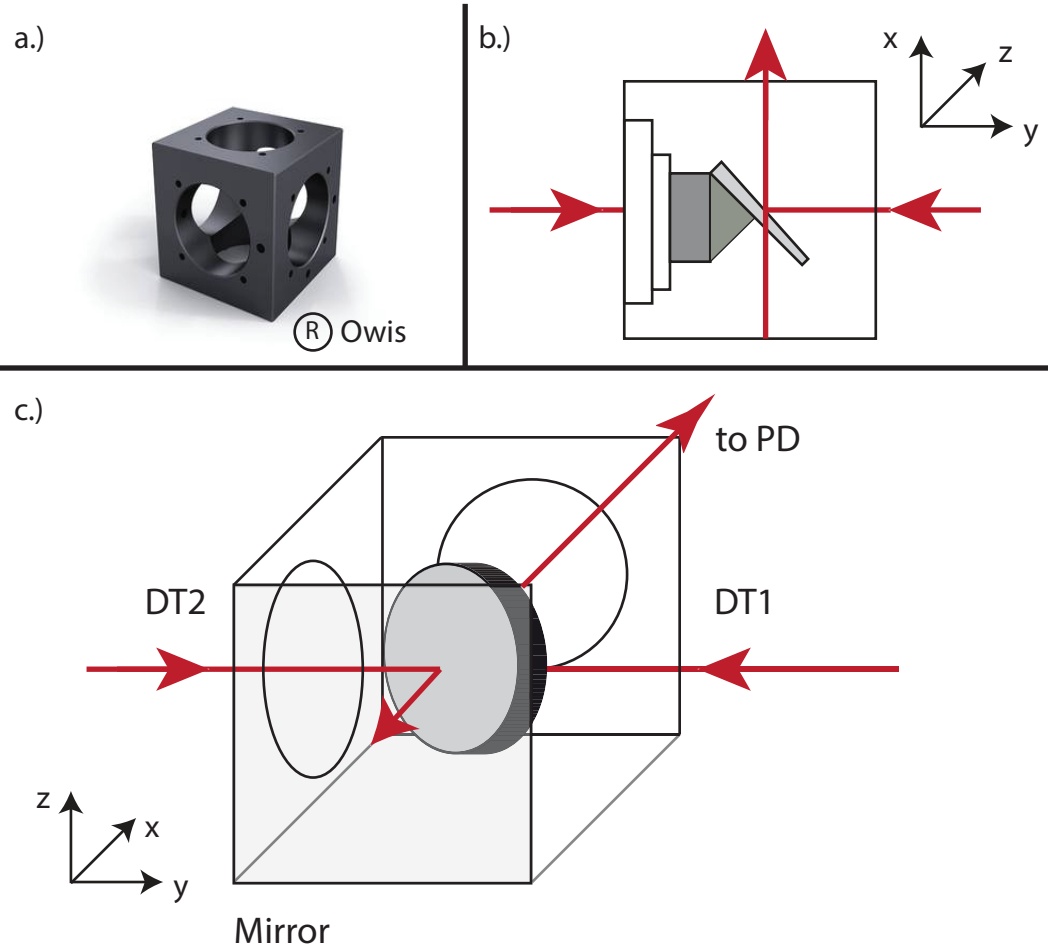
a.)

b.)

c.)

Fig. 3.2: Illustration of the interferometer built as a compact cube which can be mounted
stable such that no additional noise is added. a.)shows an image of the cube, b.) and
c.) illustrate how the wedged glass plate used for overlapping DT1 and DT2 is
inserted in this cube.

reflected upwards to the same photodiode by the reflecting side. Accordingly the power P in
the output of the cube is $P = 0.09P_{in}$ per beam. Both beams are superimposed and generate
a beat signal. This beat signal is recorded by a Thorlabs PM-400 photodiode. The expected
amplitude is according to the relative phase difference between both arms. Referring to Eq.
3.4 the intensitiy of the beat signal is $I \propto V \cos(\Delta\phi)$. Given the relation

$$\Delta\phi = \frac{2\pi}{\lambda}\Delta x \qquad (3.7)$$

any jitter in the common mode phase corresponds to a spatial jitter of the optical lattice.
This changes the relative phase of both arms at the point where they are superimposed.
Therefore, the contribution from common mode noise of our one dimensional optical lattice
can be measured.

Interference Constrast and Sensitivity

The quality of the overlap of the beams can be determined by the interference contrast or
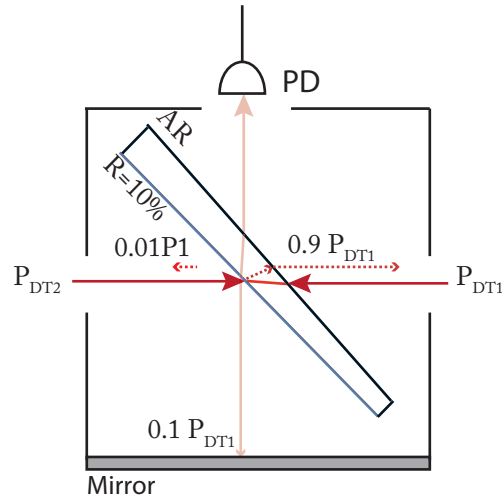fringe visibility V. In case the intensities are equal($I_1 = I_2$) the amplitude of the beat signal

Fig. 3.3: Schematic of the interferometer cube showing the beam path and the corresponding fractions of the beam powers creating the beat signal
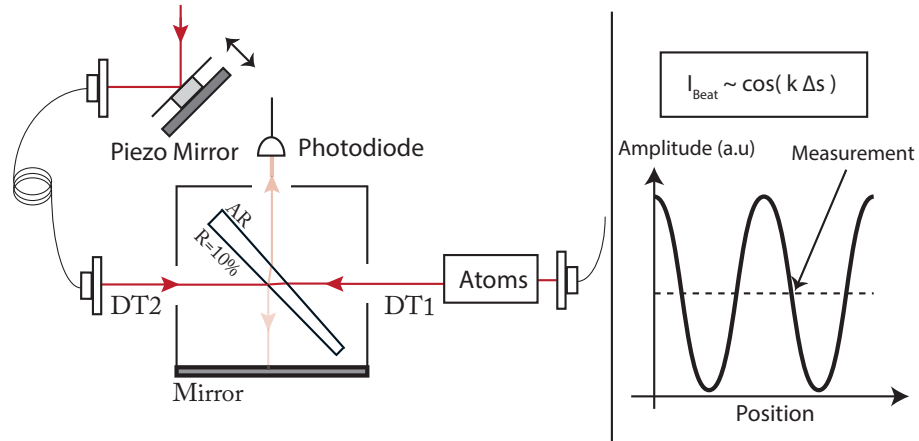

Fig. 3.4: a.) Illustration of the position of the piezo mirror, which is driven by a high voltage amplifier. Fibre coupling and intensitiy stabilization ensure that changes of the beam path yb the piezo mirror does not affect the overlap of the beams b.)This figure shows the cosinusodial interference pattern one can see on an oscilloscope when the relative position(phase) between both arms is scanned for $2\pi n$ by driving the piezo miror. It illustrates the condition of the relative phase for a measurement with highest sensitivity as well.

would reach the numerical limit of 1 for the contrast for a maximal overlap. Therefore, we measured the power of the arms by blocking the other one. For DT1 and DT2 we measured

$$DT1 : (1.53 \pm 0.01)\,\text{mW}$$
$$DT2 : (1.56 \pm 0.01)\,\text{mW}$$

From these values one would theoretically expect a constrast of

$$V_{\text{theo.}} = (0.999 \pm 0.015) \tag{3.8}$$

In order to determine the visibility experimentally, we scanned the relative optical phase $\Delta\phi$ e.g the path length of one arms (Eq.3.7) by varying the voltage applied at the piezo
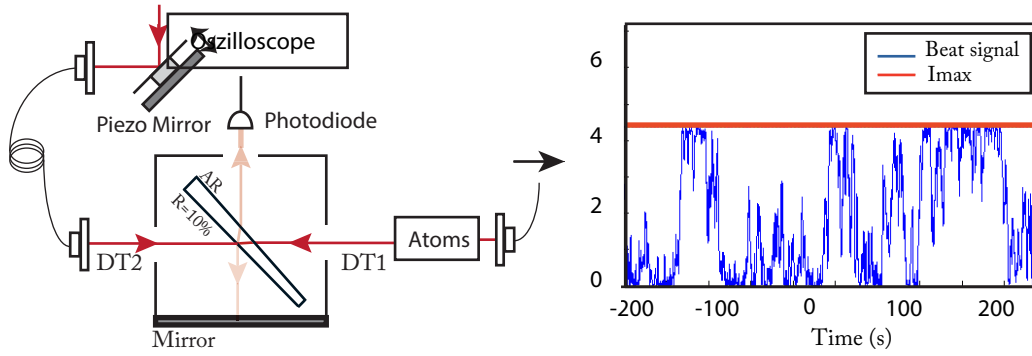
Fig. 3.5: a.) Schematic of the setup to measure temporal drifts. The piezo mirror controls the
optical phase of DT2. The interference signal is recorded by a photodiode and
displayed by an oscilloscope b.) Observation of temporal drifts in a time interval
(8min) much shorter than the data aquisition time for later measurements (45min)

mirror. The minimum and maximum voltage measured during that scan was recorded by a
photodiode. We obtained $U_{max}^{PD} = (4.37 \pm 0.01)\,V$ and $U_{max}^{PD} = (0.01 \pm 0.01)\,V$. According
to Eq.3.6 the interference contrast yields:

$$V_{\text{exp.}} = (0.995 \pm 0.011) \tag{3.9}$$

This value is in good agreement with theoretical maximum from before. In order to measure
the common mode optical phase noise as precise as possible the interferometer is supposed
to operate at a point where the sensitivity to changes in the relative phase is maximal and
(ideally) linear for small changes. According to Eq.3.3 this is the case for,

$$\frac{\partial I_{all}}{\partial \Delta \phi} = 2\sqrt{I_1 I_2}\sin(\Delta \phi). \tag{3.10}$$

which means for $I_{all} = 0$. Therefore the piezo mirror was used to find an appropriate position
which fulfilled that condition before the first measurement of the relative phase noise had
been done.

3.3.1 Supression of temporal drifts

For a reliable measurement of the phase noise the interferometer is supposed to operate
during the whole data aquisition time with a constant, maximal sensitivity. Therefore we
studied first the temporal behaviour of the beat signal using an oscilloscope. The measure-
ment setup and the corresponding result is illustrated in Fig.3.5. The piezo mirror had been
adjusted such that the beat signal meets the point with maximal slope before. Without any
common mode phase drifts one would expect a constant signal around $U_0 \approx 2.2\,V$.

However the temporal trace of the intensity reveals fluctuations between the minimal and
maximal values $U_{min}^{PD} = (0.01 \pm 0.01)\,V$ and $U_{max}^{PD} = (4.37 \pm 0.01)\,V$ respectively. This mea-
surement shows that we have common mode optical phase drifts on the order of 2π on a
timescale of minutes. The photodiode we used saturates at 9 V. According to the voltages
in Fig.3.5 we can be sure that we are using the photodiode within the correct power input
range. This measurement reveals that it is necessary to extend the setup with an additional
control loop to suppress the recorded slow drifts of the optical phase. As it is illustrated in
Fig. 3.6 this has been realized by dividing the signal behind the photodiode. One is used for
the measurement of the phase noise and the other for the feedback loop of the piezo mirror.
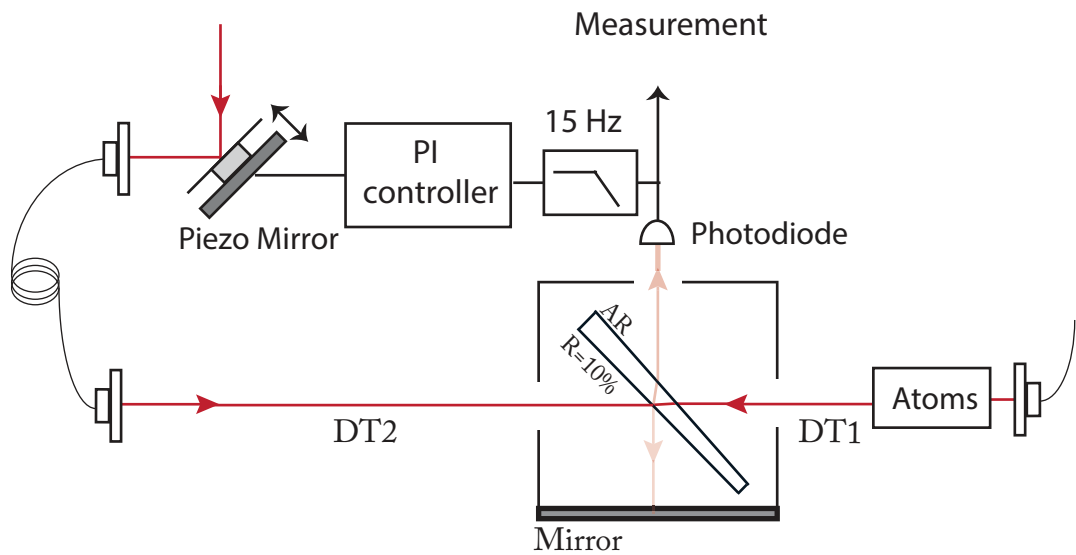
Fig. 3.6: Setup of the addition of the system for compensation of the temporal drifts shown in Fig.3.5. It consists of a low pass filter to generate a slow loop and the corresponding PI control. The signal from the photodiode serves as an error signal. The output of the PI control is the input of the piezo mirror.

The beat signal with these intensity fluctuations serves as the input of a PI controller. The PI controller generates a correction signal which is fed back to the driving input of the piezo mirror. The piezo mirror is driven by a high voltage. This serves as the actuating variable of the loop because that voltage is used to modulate the position of the piezo. Accordingly the optical phase delay of DT2 is modulated.

This stabilization loop should only compensate the slow drifts of the optical phase and also keep the optical phase at the point of the highest sensitivity. This is for the same reason the ideal lock point as well.

Therefore an additional low pass filter with a cut off frequency of $\nu_c = 15\,\text{Hz}$ has been inserted before the signal enters the PI controller. Thus long term drifts are compensated and the AC component can be measured.
It is expected that the amplitude of the phase noise between the measurement without the loop and the loop differs by $3\,\text{dBm}$, because the averaged intensity of the interferometer has an factor of 2 which corresponds to $3\,\text{dBm}$ (c.f Fig.3.4 b.)).

3.4 Power Spectral Density (PSD)

The common mode optical phase noise leads to a fluctuating intensity of the beat signal. Thus, it is measured as a temporariliy fluctuating voltage on the photo diode in Fig3.6. This signal was transmitted to a network analyzer, which rather recorded the power spectral density spectrum. In order to connect both quantities I will derive an expression for the power spectral density and partly following the derivations in [54],[9]. A noise value of a quantity cannot be predicted deterministically but is rather described by the corresponding probability distribution. In case of randomly distributed events, the distribution is determined by

the mean and the variance.[1] In addition the Fresnel-Huygens principe states that a signal can be regarded as a superposition of all single spectral components of a variable in time space [46]. That corresponds to the Fourirer decomposition of the voltage into ist spectral components. Expressed as the Fourier transform yields:

$$V(\omega) = \frac{1}{2\pi} \int_{-\infty}^{\infty} V(t)e^{i\omega t}dt \qquad (3.11)$$

For a finite measurement of duration T this can be written as:

$$V(\omega) = \frac{1}{2\pi} \int_{-T/2}^{T/2} V(t)e^{i\omega t}dt \qquad (3.12)$$

However a device as a spectrum analyzer rather measures the averqage transmitted power in discrete steps of certain bandwidths, i.e frequency intervals, than the voltage . [54]. This results in a power spectral density spectrum, which delivers the information about the fractional amount of total power per frequency interval by the power spectral density. The average generalized power in one interval can therefore be written as:

$$\langle P \rangle_T = \langle V^2 \rangle_T = \frac{2\pi}{T} \int_{-\frac{T}{2}}^{\frac{T}{2}} |V(t)|^2 dt, \qquad (3.13)$$

since $V_T(t)$ is a real valued quantity, the spectrum an even function. Referring to Parseval's theorem [56] the energy of a signal in time domain is equal to the one in frequency domain. In mathematical terms this means that the L2-norm of the Fourier transform of the modulus squared is the same [56].

$$\int_{-\infty}^{\infty} |V(t)|^2 dt = \int_{-\infty}^{\infty} |V(\omega)|^2 d\omega \qquad (3.14)$$

and $V_T(\omega) = V_T^*(-\omega)$. Therefore utilizing Eq.**??** and 3.14 the expression for the total power can be written in the limit for $T \to \infty$ as:

$$< P_{\text{all}} >= \int_{0}^{\infty} S_v(\omega)d\omega \qquad (3.15)$$

with the portion of the total power spectral density(PSD) function defined as [9]:

$$S_v(\omega) = \lim_{T \to \infty} \frac{4\pi}{T} < |V_T(\omega)|^2 > \qquad (3.16)$$

Therefore $S_v(\omega)$ corresponds to the portion of average power of the signal $V(t)$ in a frequency interval $d\omega$

3.5 Measurements and Results

Using a networkanalyzer (NWA) we measured the power spectral density sprectrum over six frequency decades from 1 Hz to 1 MHz. One measurement took approximately 45 minutes and all results are displayed as Bode-Plots in semilogarithmic scale. In the following the results are presented and discussed
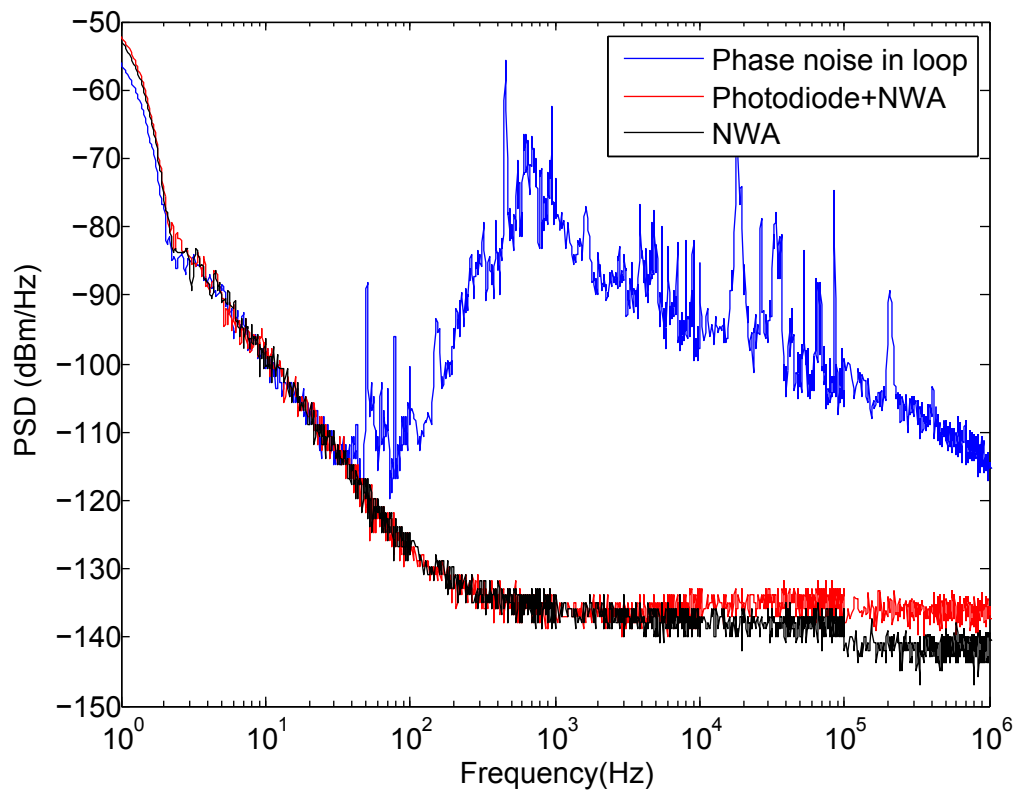
Fig. 3.7: PSD of the common mode phase noise in loop due to the common mode movement of the optical lattice. Moreover the corresponding noise floor the networkanalyzer and of the photodiode, which also contains the NWA noise floor was measured.

In order to know the limit of our measurement, that is the noise floor, we first recorded the PSD of the NWA itself and then with a blocked photodiode. The latter contains both the background noise from the NWA and the photodiode.

As one can see in Fig.3.7 the noise floor from the NWA and the photodiode differs insignificantly. Thus only the signal from the photodiode is used as a noise floor in further plots. The noise floor dominates the spectrum up to 1 kHz. Referring to this one can see in the frequency range of up to 1 kHz that the noise amplitude from the photodiode and the networkanalyzer is on the same level. Towards higher frequencies the noise level of the networkanalyzer is even below the photodiode's level. However, since the curves are quite similar, far below the amplitude of the measurement of the common mode phase noise and the photodiode contains the noise floor from the photodiode as well, only the signal from the photodiode will be used as a noise floor in further plots.

In the low frequency region to tens of Hertz $\frac{1}{f}$ noise is dominating and for the photodiode it is the ruling term up to 100 Hz [6]. In the region between 1 kHz and 10^6 Hz they reach a constant noise level(white noise). In the graph of the common mode optical phase noise of the optical lattice the peak and its harmonice around 50 Hz is caused by the power grid. The distribution is broadly peaked between 500 and 1500 Hz with values up to -65 dBm/Hz. Towards higher frequencies the general level decreases to amplitudes between -100 and -120 dBm/Hz. The mean value of the background noise is at -127 dBm/Hz and the one of the phase noise in loop at -97 dBm/Hz This phase noise which has its main contribution in the acoustic range can be, for instance, due to mechanical vibrations of the optical table and corresponding optics.

3.5.1 Phase and Intensity noise contributions

It is not possible to distinguish (from the result shown in Fig.3.7) between pure phase noise and contributions due to intensity noise. Therefore we recorded the power spectral density spectrum for the intensity noise of DT1 and DT2 individually on the network analyzer. As is is shown in Fig.3.8 the contribution from the measurement with the interference signal in loop dominates the spectrum over the whole frequency range since the PSD values from DT1 and DT2 respectively are much lower. Since the lattice arms are both generated by the same source, the Ti:Sa, the general noise is as expected similar.

From Fig.3.8 we can conclude that the main contribution of the noise is indeed due to the common mode phase noise of the optical lattice.

3.5.2 Comparison of phase noise in loop and out of loop

Fig.3.9 compares the measurement of the relative phase noise once measured while the optical phase noise is kept constant as desribed in Sec.3.3.1 and once without the loop . Comparing the mean values of the phase noise for both cases yields that as expected the sensitivity is increased. The mean value of the measurement out of loop is -100 dBm/Hz and displayed in Tab.3.1 as well. As expected the amplitude is generally increased by 3 dBm/Hz for the in loop measurement of the phase noise. Thus the interferometer is operated at maximum sensitivity without adding noise by the feedback loop and due to the slow lock we measure the AC component of the phase noise.
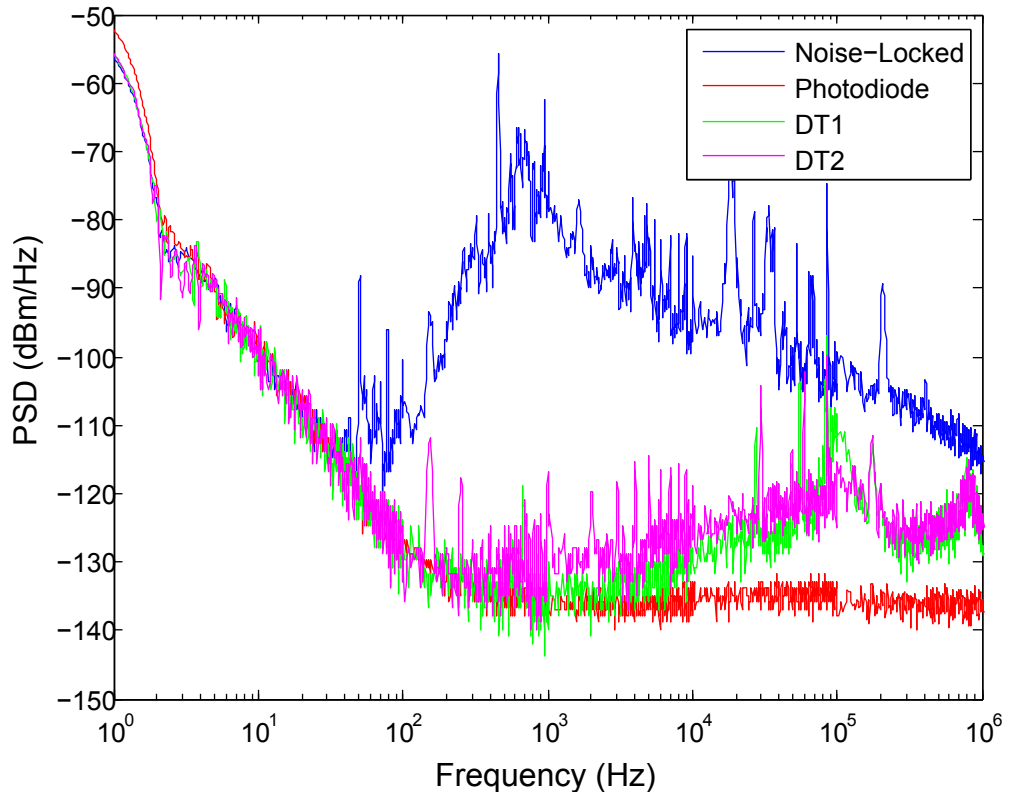
Fig. 3.8: The noise signal is plotted together with the PSD spectrum from DT1 and DT2. The amplitude of the measurement with the inteferometer is well above the contribution from DT1 and DT2. For low frequencies (<1 kHz) the amplitude from DT1 and DT2 is on the background noise level. Both arms own a very similar noise behaviour over the whole frequency range

3.5.3 common mode phase noise in units of lattice sites

As it is illustrated in Fig.3.5 the phase scan revealed a maximum voltage of $V_{\text{max.}} = (4.37 \pm 0.01)\,\text{V}$. This corresponds to a phase of $\frac{\pi}{2}$ or a distance of half a lattice site $d = \frac{\lambda}{2}$. Referring to Fig. 3.10 the phase noise Δphi can be expressed from the ratio:

$$\Delta\phi = \frac{V_{\text{jitter}}^{\text{RMS}}}{(V_{\text{max}}/2)} \tag{3.17}$$

Further, using Eq.3.7 yields the following expression for the stabilized optical phase noise in spatial units:

$$\text{x} = \frac{\text{d}}{\pi(V_{\text{max.}}/2)}V_{\text{jitter}} \tag{3.18}$$

In addtion the power spectral density $S_v(\omega)$is proportional to the power and using Eq. 3.13 the relation to the measured quantity is then:

$$\text{x}^2 = \left(\frac{\text{d}}{\pi(V_{\text{max.}}/2)}\right)^2 \cdot S_v(\omega) \tag{3.19}$$

---

[1]Assuming a gaussian normal distribution and using probability theory, that a probability distribution is determined by the (ruling) stochastic moments. [55]
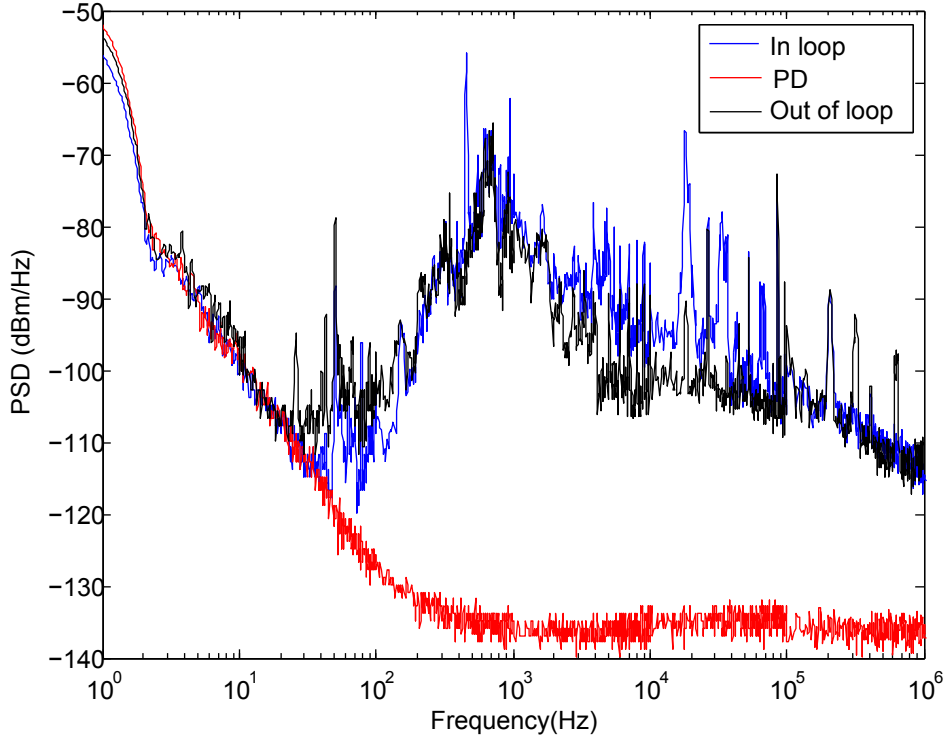
Fig. 3.9: Noise from the light field of the dipole trap in the unlocked and the locked case. Since the lock increases the sensitivity for the noise the amplitude from the measurement with a lock is increased by 3 dBm/Hz (c.f. Tab 3.1).

Therefore we obtain the RMS values of the common mode optical phase noise in nanometers for the stabilized case. An estimation for the case with the feedback loop cannot rely on a mean value but has been rather weigthted with respect to the single contributions.

$$\textbf{In loop}: x_{RMS} = (44 \pm 5)\,\text{pm} \tag{3.20}$$

$$\textbf{Ratio to lattice site}: \frac{(1.02 \pm 0.12) \cdot 10^{-4}}{d} \tag{3.21}$$

The contribution of the AC component of the common mode phase noise of the optical lattice is four orders of magnitude smaller than one lattice spacing of $d = 433\,\text{nm}$ on the timescale of one hour since one measurement of the PSD lasted approximately 45 min. All in all the contribution of the AC component of the the common mode phase noise from

	Mean amplitude (dBm/Hz)
In loop	-97
Out of loop	-100
Background noise	-127
Difference : 3 dBm/Hz	

Tab. 3.1: Mean values of for the case with and without the feedback loop
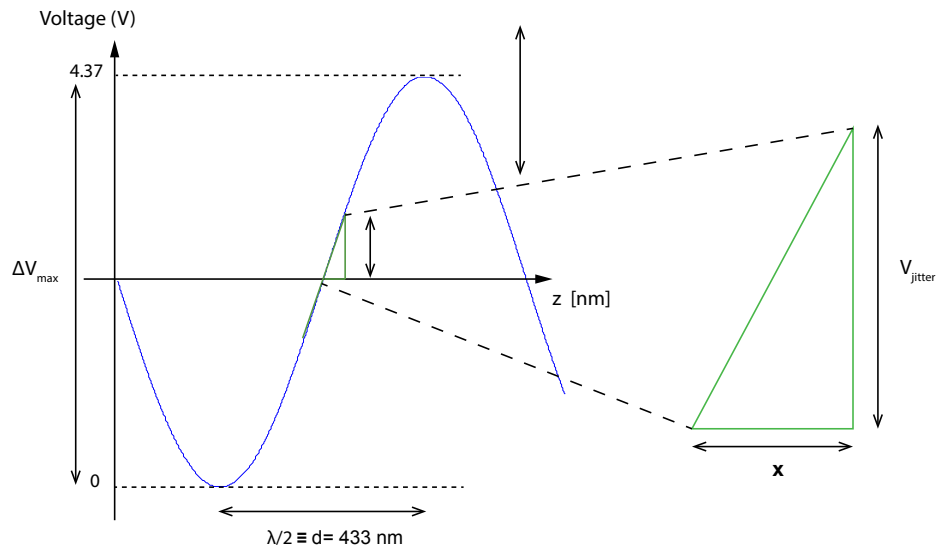
Fig. 3.10: Illustration for the derivation of the RMS value of the common mode phase noise in units of lattice sites a.
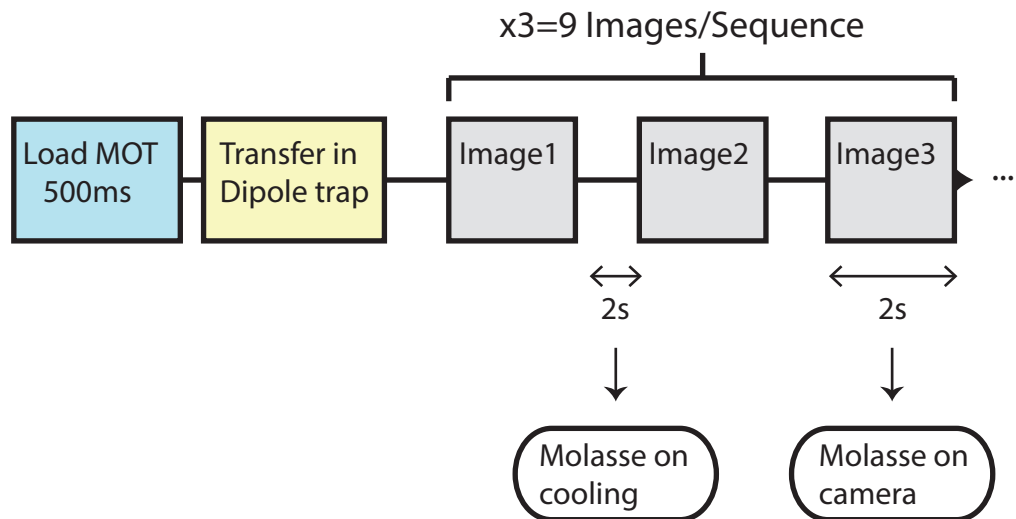

Fig. 3.11: Schematic representation of one experimental sqeuence for obtaining the images. Each sequence produced 9 images, was repeated 1000 times. Thus it resulted in a total of 9000 images. This was done with and without lock. In order to have only few Atoms, atoms are loaded into the MOT for 500ms, then transferred into the dipole trap, and then the first image is taken. Referring to this taking an image and the break in between tooks 2s each.

the optical lattice has been characterized so far. In the following I will focus more on the slow drifts and how these may affect the position reconstruction.

3.6   Analysis of Displacements of Atoms

Experimental Sequence

In order to analyze the influence of the common mode movement of the optical lattice on the imaging of the atoms position we took a series of images with the CCD camera. Using an analysis software which has been previously written in our group in Matlab by Andrea Alberti I analyzed the displacements of the atoms' positions between different images, i.e lattice drifts.

As it is also demonstrated schematically in Fig.3.11 one sequence is divided into several steps. First we loaded for a time of 500ms atoms into our **M**agneto-**O**ptical-**T**rap (MOT). As a result, only few atoms were loaded into the dipole trap, which allows to trace the position of individual atoms over time. In the next step the atoms are transferred into the dipole trap [26, 21]. There the atoms can be detected and counted by using fluorescence light impinging on an EMCCD camera creating the images [38]. For further analysis,e.g. extracting the atoms' positions the raw data is processed to the computer. As soon this step is finished the first image is taken within 2s. Then we wait for 2s and take the next image. In total within one sequence nine images are taken. The molasses is set on the camera options during the time of taking an image in order to maximize the fluorescence detection and in the break between on cooling parameters to reduce effects from heating. For more statistics that sequence was iterated for 1000 times which resulted in a total of 9000 images for the case with and without the feedback loop for stabilization and removing the DC component of the phase noise turned on.

 Fig.3.12 a.) shows exemplarily one image from the measurement. Over the total image width of 313 binned pixels one can identify two atoms. In b.) the distribution of photoelectron counts, the detection threshold and the single regions of interest (ROI) are displayed.

Software Analysis Steps for Obtaining the Positions of the Atoms

For each image the software first substracts an offset and generates the ROIs when the photoelectron counts exceed a threshold. For the imaging time which is used her, the threshold is set at 50 photoelectron counts [38]. Referring to Fig.3.12 20 additional pixels have been added to the ROI. If one integrates over the ROI in all images and bins the result in a histogram one obtains a rate of 1000 photolectrons per atom per second. The number of atoms in each ROI is determined by integrating the binned intensitiy distributions. [38]. The data was taken with slightly worse illumination settings than usual. Usually one obtains around 2000 photoelectrons per atom per second. Nevertheless the analysis of the displacement is not affected by that.

The following description is based on the work of M. Karski described in his PhD-thesis. Thus further information can be found in Ref.[38]. All the data is extracted from fluorescence images of the atoms using a EMCCD camera. If the atoms would be described as an ideal, pointlike object and no imperfections such as dicrete sampling and noise of the imaging optics present, the response of the imaging apparatus would simply described by the point spread function (PSF). In case of purely diffraction limited optical system the form of the PSF corresponds to the Airy, disc [53]. However, with finite resolution powers, discrete sampling of EMCCD camera and atoms rather represented as a thermal wavepacket, the recorded image is blurred.

The line spread function (LSF)

We are rather interested in determining the response function of the atoms in one dimension along the optical lattice. Further the atom is smaller than the provided resolution in the one
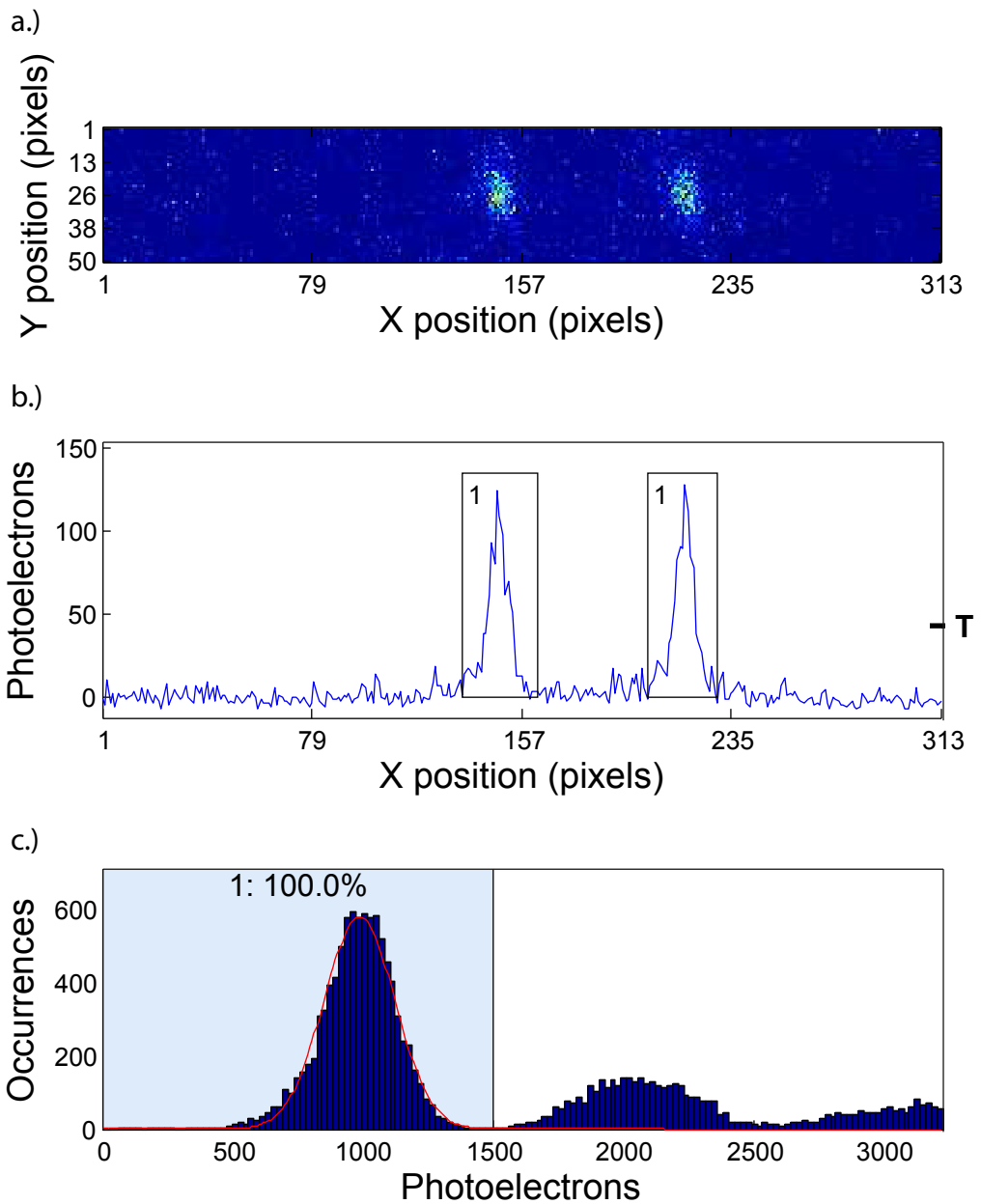
Fig. 3.12: a.) This is an example for all the images we obtained with the scaling in pixels. One can two strong fluorescence signals corresponding to detected atoms b.) That plot shows the integrated number of photoelectrons per ROI of a width of 20 additional pixels with a detection threshold for at least one atom of 50 CCD counts. c.) Histogram of the integrated number of photoelectrons per ROI for all images. Here we constrained the detection to one atom per ROI for the analysis of the displacements. Successful detection takes place at 1000 photoelectrons per atom per second.

dimensional case. Therefore we rather consider the line spread function (LSF) $L(x)$, which is defined as the convolution of a delta function with the two dimensional PSF:

$$L(x) = \delta(x) \star P_{2D} \qquad (3.22)$$

In mathematical terms, the recorded image is a convolution of the ideal PSF with an initial, unblurred intensity distribution.

$$I(x) = L(x) \star I_0(x) \tag{3.23}$$

Thus, the initial image has to be reconstructed from the recorded one which is known as a deconvolution process. [57] Following Ref.[38] the positions of the atoms is determined by means of parametric deconvolution.[2]. However, the corresponding LSF has to be well determined. Therefore the accurate reconstruction of the LSF is an important prerequisite for the determination of the position of the atoms. Without going to much into detail it is determined in the following steps. [38]:

1 Consider N single isolated atoms with axially binned discretly sampled intensity distributions I_N

2 Assume initial model function $L(x)$ roughly approximated by gaussian shaped intensity distribution

3 Determine position by minimizing difference between quantities from 1 and 2

4 Approximate discrete intensity distribution by a continuous one and sum all N intensity distributions

5 Continue untilset convergence criterium is reached

6 Increase accuracy by 'self-consistency' loop of LSF, i.e replace modeled LSF by new, refined LSF $\tilde{L}(x)$

The LSF is then used to analyze the position of the atoms in a Gaussian fit. The accuracy of the determination of the LSF and thus the parametric deconvolution is influenced by drifts of the optical lattice relative to the imaging optics. The common mode optical phase noise corresponds to such a drift. Therefore the LSF is extracted from the data for both the stabilized and unstabilized case. In the unstabilized case we expect thath the phase can drift up to one lattice site during an illumination time of 2 seconds without the feedback loop. (c.f Fig.3.5) However this corresponds to a change of $d = 433\,\text{nm}$ which is still smaller than the resolution [38]. Therefore we expect, that the LSF generated with the feedback loop differs marginally from the case without the feedback loop.

Result

The images were analyzed by using the analysis software in matlab code as described above. As it is illustrated in Fig.3.13 the result conincides with our expectations. It is not possible to see a difference with bare eyey and the full width at half maximum(FWHM) of the corresponding fit yields:

This histogram is shown in Fig.3.12 c.). The exact positions of the atoms in one ROI image are determined by fitting gaussians curves with the position represented by the center of that gaussian. In the course of this 1.471 pixels correspond to one lattice site. At this point it is now possible to analyze the displacements between different images.

As it is shown in Fig.3.13 the LSF's are up to small broadening for the case with the feedback loop very similar. From the analysis we obtained information about the full width at half maximum (FWHM).

$$\text{FWHM}_{\text{LockOFF}} = 7.713\text{px} \tag{3.24}$$

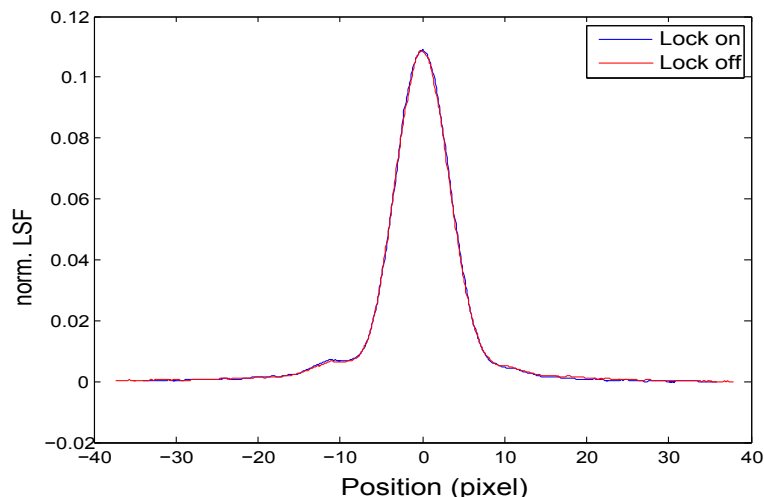[2]For more information see reference therin, as well

Fig. 3.13: This graph displays the normalized LSF both when the feedback was turned on and off. For the case out of loop the FWHM was at 7.713 px [2.234 microns] with a strehl ratio of 0.771. In case with the feedback loop we obtained for the FWHM 7.778px[2.252 microns] and a strehl ratio of 0.772. The FWHM for the case in loop is slightly higher since the sensitivity to the phase noise is higher. *%*

$$\text{FWHM}_{\text{LockON}} = 7.778\text{px} \tag{3.25}$$

In Abbe units these values correspond to 2.23 and 2.25 micrometer respectively. This result is in accordance with our expectations.

Taking the previous discussion into account there still remain some questions. Does that common mode movement of the optical lattice lead to some drifts of the position of the atom regarding its initial position over time? And if there is a drift, on which order is the drift.

These questions will be tackled in the following by looking at the reconstructed atoms position comparing the first image to the second and the first to the ninth image. The results will be then binned into histograms of the displacements in units of the initial position.

3.6.1 Displacements of the atoms' positions

In the analysis I concentrated on two cases since they represent the most distinct ones. First I determined the displacement between two successive images, i.e the displacement between the second and the first of one sequence, as described in Fig. 3.11. This represents the minimal time distance. Then I also considered the maximum time difference, that is the displacement between the last(ninth) and first image. Including the pause the minimal time between two images is $\Delta t_{\text{min}} = 4$s and the maximum time $\Delta t_{\text{max}} = 36$s. All histograms which are shown in the following are normalized to the total number of images.

In order to reveal also small shifts in the position with respect to a previous image the histograms are binned in steps of 0.25 lattice sites.

The displacement was calculated assuming that during the time between the considered images the same atom was recorded in the initial position. Therefore, if the displacement was bigger than two pixels, it was assumed, that the compared positions belong to two different atoms. [3]

---

[3]The LSF and thus the position is determined with sub pixel precision, therefore this assumption is valid.
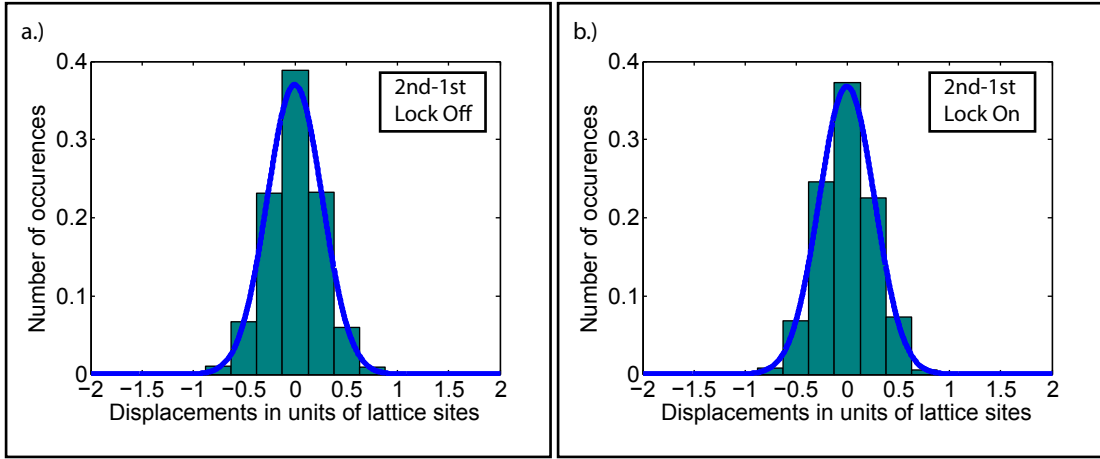
Fig. 3.14: Histogram and a gaussian fit for the displacement of an atoms position from the first to the second image without a.) and with the feedback loop. The time difference between the compared images was 4 s. The distributions are clearly peaked at zero (Tab.3.2).

Fitparameter	LoopOFF	LoopON	LoopOFF	LoopON
	2nd to 1st		9th to 1st	
μ	(0 ± 0.01)	(0 ± 0.01)	$-(0.02\pm0.01)$	(0 ± 0.01)
FWHM	(0.63 ± 0.01)	(0.64 ± 0.01)	(1.05 ± 0.02)	(0.76 ± 0.02)

Tab. 3.2: Mean and FWHM of the Gaussian distributions in the histograms for the analysis of the displacements

The displacement is expressed in units of lattice sites to achieve a better measure for the influence of this fluctuations to the single site resolution. In addition all histograms are plotted together with a fit of gaussian function to the distribution. The corresponding mean values and widths are displayed in tab.3.2. Fig.3.14 shows the distribution of the displacements with and without the feedback loop for the comparison of the second with the first image of one sequence. A comparison of the distribution of the displacements with (Fig.3.14a.) and without the feedback loop reveals that the slow drifts the loop stabilizes for do not influence the distribution. Thus, these drifts do not affect the single site resolution on a time scale of 4 s. The Gaussian form of the distribution corresponds with what we would expect from our resolution from the imaging optics [29, 38] and the statistical fluctuations along one lattice site. This can be clearly seen in the FWHMs of the corresponding fits. (c.f. Tab.3.2). For this case the spread of the positions of the atoms has within the errorbars the same value. The situation changes when the displacements between the ninth and the first images are considerd. The result is presented in Fig. 3.15 a.) without and b.) with the feedback loop turned on. Compared to before the distribution in case of being out of loop is much broader. Referring to Tab.3.2 the mean of $\mu = -(0.02\pm0.01)$ indicates now a drift of the center position of the distribution to the left with a FWHM of (1.05 ± 0.02). Thus, the slow drift of the common mode optical phase affects the reconstruction of the positions of the atoms on the timescale of 36 seconds. The influence of the slow drift is verified by the plot of the measurement with the stabilization loop. (c.f Fig. 3.15) b.). Using the feedbck loop
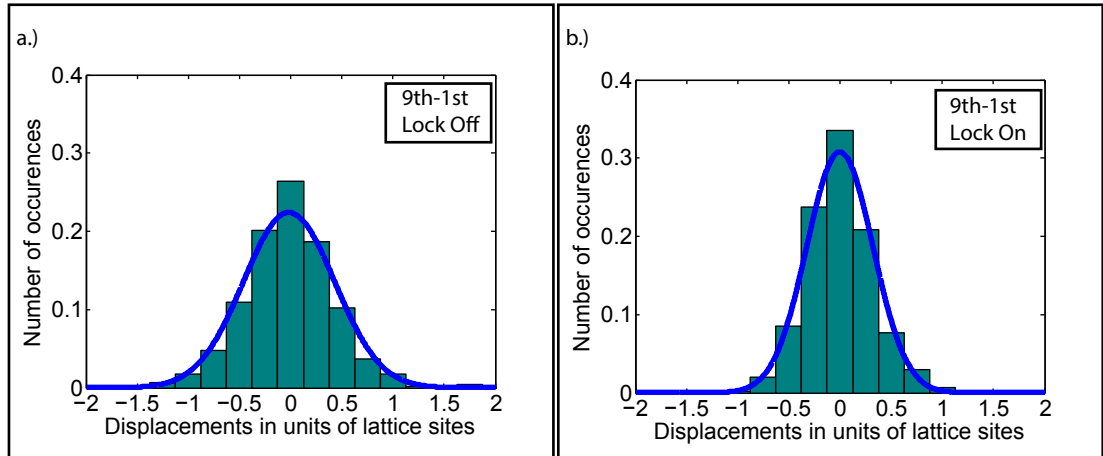
Fig. 3.15: Histogram and gaussian fit for the displacement from atoms from the first and the last (ninth) image in one sequence without (a.)) and with(b.)) the loop turned on. The time between these images was 36s which is the largest time distance. One can see that the lock minimized the spatial drift of the optical lattice ($\approx$ 30%) A similar distribution to the first case is recovered by the loop.

reproduces the distributions shown in Fig. 3.14 a.) and b.).[4]

3.6.2 Summary

In this chapter I characterized the optical phase noise due to a common mode movement of the optical lattice. This noise contains a fast and a slow component. The fast one could lead in principle to heating or decoherence of the atoms, while the slow can affect the accuracy of the position reconstruction [28, 6]. The fast component corresponds to a spatial jitter as well and has been measured by recording a power spectral density spectrum. Accordingly a slow feedback loop (15 Hz cutoff frequency) was added, which supressed the slow drifts. From the power spectral density spectrum with the feedback loop the RMS value was calculated in units of lattice sites It is $x = (1 \cdot 0.1 \pm 10^{-4})$ d. The jitter is thus several orders of magnitude smaller than one lattice spacing. In order to study the influence of the slow drift on the position reconstruction of the atoms a series of images has been taken. The comparison of the linespread function showed no difference between the case with and without the loop. This agrees well with the expectation, since the phase could drift up to one lattice site during the illumination time of 2 seconds.(Fig.3.5) This is in the order of 433 nm and thus it cannot be seen in the LSF. Additionally the displacements between two images for times of $t = 4(36)$ s have been analyzed to find the timescale when the drift influences the position reconstruction. As it is illustrated in Fig.3.15 and Tab.3.2 the drift changed the distribution of displacements on a timescale of 36 seconds. The usage of the feedback loop removed the contribution of the drift and the distribution is comparable to the ones for a time difference of 4 seconds. Atom operations and state dependent transport are much smaller than this time, which means that the slow component is not affecting the analysis on that timescales. In the scope of this thesis all aspects of this phase noise could not be covered but to obtain a complete understanding of the effects from the differential movement of the phases of the standing wave potentials should be considered as well in the future.
However a stabilization of the fast fluctuating component could increase the situation and

---

[4]Since the time interval was increased the distribution is still broader due to the statistical spread than the figure from the analysis of subsequent images.

stabilize both components from the common mode phase noise of the optical lattice. This would require an independent control and tracing of the temporal evolution for both lattice potentials individually. Therefore the next chapter presents first considerations into an extension of the phase noise interferometer to a quadrature interferometer.

4

Quadrature Interferometer

Referring to Sec.3.6 the feedback loop stabilized the slow drifts of the optical lattice. As a long-term goal the fast component of the optical phase noise should be stabilized as well. However, it requires a different setup, because it should not influence the state dependent transport. The slow feedback loop can not follow on the timescale of the transport. The state dependent transport is realized by controlling the relative phase between an optical conveyor belt each for the σ^+ and σ^- lattice potentials. [50].By means of an conveyor belt atoms are transported over several lattice sites. It has been demonstrated first in 2001 by Stefan Kuhr. [28]. The corresponding phase stability is achieved by direct polarization synthesis[50]. Therefore it is necessary to control both components and measure the temporal evolution of the phase noise individually for the σ^+ and σ^- polarized lattice. A possibility is to extend the phase noise interferometer from Chapter 3 to a quadrature interferometer. In contrast to the quadrature measurement presented in Sec.2.5, the in-phase component $I(t)$ and the delayed quadrature component $Q(t)$ are both interference signals from the corresponding beams. The phase noise interferometer has to be modified to produce two interference signals with a relative phase difference of $\frac{\pi}{2}$. Thus, I will explain the general idea of this quadrature interferometer. Further I will show first considerations regarding stability and implementation into the experiment.

4.1   Experimental test apparatus

For that setup a littrow laser at 852 nm served as the light source(Fig.4.1). An uncoated glass plate (N-BK7, $\varnothing = 25$ mm with a thickness of 5 mm is inserted instead of the wedged glas plate in case of the phase noise interferometer. Therefore the light is reflected and transmitted both from the front and the back side of the glass plate. As it is shown in Fig.4.2 this creates two beams with a relative phase delay. As it is illustrated in Fig.4.1 the interference of the front and the back pair is generated by two mirrors. One mirror is fixed and the other one is a piezoelectric-actuated mirror. This allows to scan over a complete phase period of 2π. According to Sec.2.5, when I(t) and Q(t) are in quadrature it is possible to visualize the phase evolution on a circle. The signals are separated by means of a D-shaped mirror. Both signals are focussed by lenses with focal length of f=60 and f=50 mm respectively. Then they are recorded by a photodiode. In this setup two different photodiodes were used. For the quadrature signal Q(t) we used a photo diode which has been built in the institute. For the in phase signal we used a commercially available Thorlabs PM-400 photodiode. The photodiodes are calibrated differently. In order to match the power levels an additional polarizer and a $\frac{\lambda}{2}$ plate are inserted in the path of the quadrature components
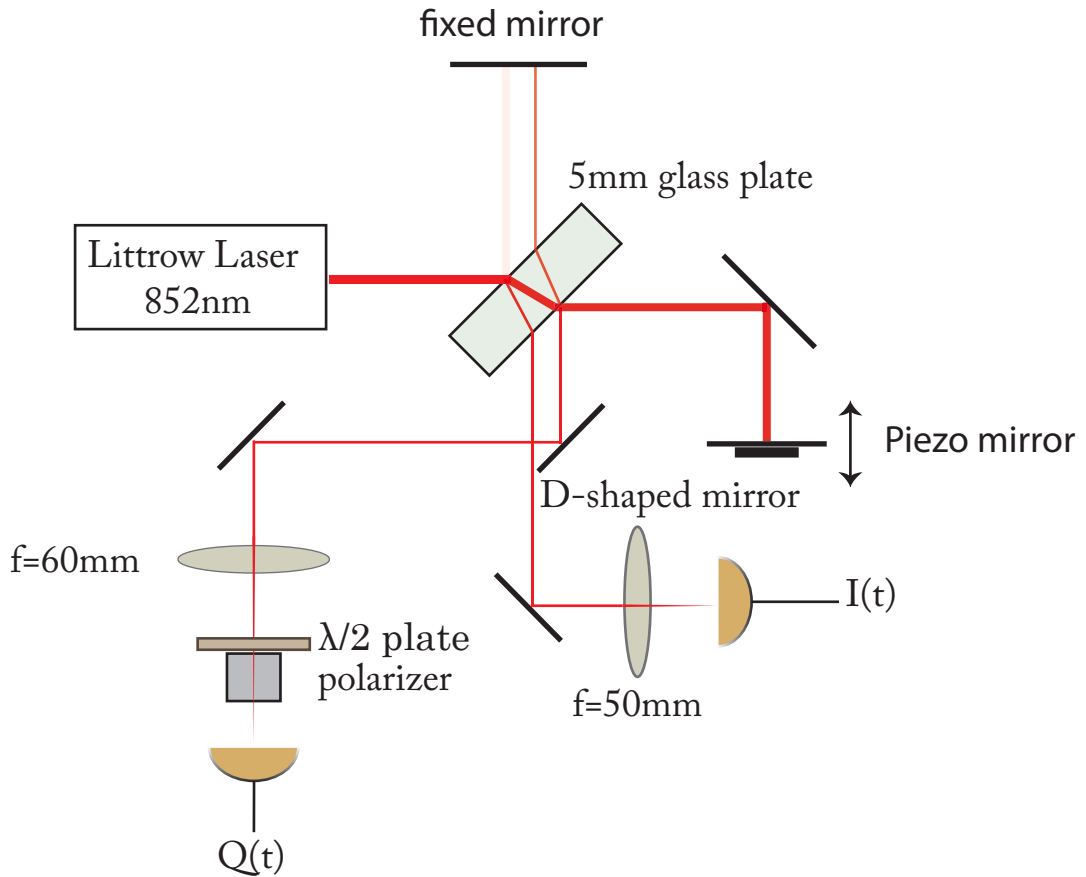
Fig. 4.1: Experimental Test Setup for first characterizations. For simplicity the additional reflected beams from the glas plate are not drawn. The glas plate both splits the laser beam into two interference arms and generates by reflection on the front and the back side the in phase and the quadrature component. A D-shaped mirror separates both components. The signals are both recorded by a photodiode. In order to ensure the same voltage level on the two different types of photodiodes (I(t):Thorlabs PM-400,Q(t): Selfmade) the power is matched by the waveplate and the polarizer.

The path length difference Δl which corresponds to the phase delay of $m \cdot \frac{\pi}{4}$ (c.f. Fig.4.2),where m denotes an integer number. If this length difference is already fluctuating in the same order, i.e in the nanometer scale,the quadrature signal would be highly unstable. Such fluctuations can occur due to mechanical vibrations or thermal flucutations, for instance. Therefore the glass plate has to be mounted with high stability and the tilt of the glass plate precisely adjusted. According to this the glass plate is mounted on a high precision mirror mount with differential adjusters (Thorlabs KS1D). The resolution by the differential adjusters is at 660 μ rad per revolution (rev). A theoretical calculation, which is in detail in the appendix yields the following expression, for the necessary sensitivity:

$$\frac{d\Delta l}{d\delta\alpha} = \frac{2h}{n^2}\left(1 \quad \frac{1}{n}\right) \tag{4.1}$$

With h=5 mm this results in $\tag{4.2}$

$$0.74 \frac{\text{nm}}{\mu \text{ rad}} \tag{4.3}$$

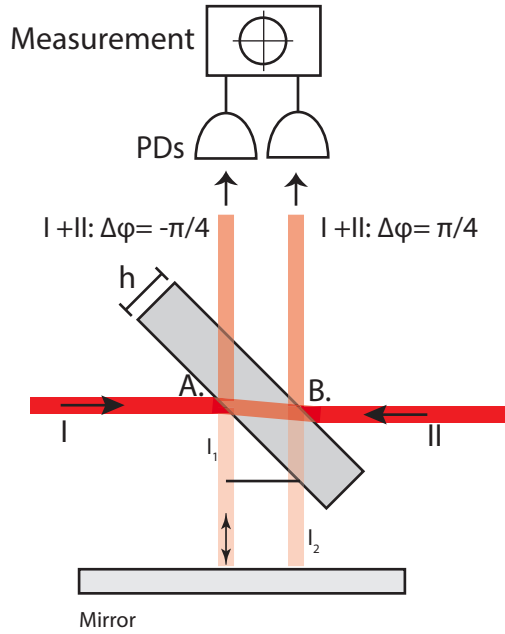where $\Delta\alpha$ corresponds to small fluctuations of the incidence angle, h the thickness and n the

Fig. 4.2: Generation of the quadrature components I(t) and Q(t). A glass plate serves as a beam splitter. The phase delay Δx corresponds to a delay of $\frac{\pi}{4}$. Both beams accumulate this delay. Since they are counterpropagating the relative phase delay results in $\frac{\pi}{2}$.

refractive index of the glass plate n= 1.5 A change of $\frac{\pi}{2}$ would correspond to approximately 290 μ rad and therefore this mount can be used for adjustment.

As illustrated in Fig.4.2 the phase delay is generated by a glass plate of thickness h. Since the beams are counterpropagating the relative phase difference of the interference signal on each side at A. and B. in Fig.4.2 of the glas plate has the same value. This phase difference is generated by the varying lengths from the overlap of a transmitted and reflected beam in A. and B. However, the sign is different. Thus, a quadrature signal can be recorded if the pathlength difference in A. and B. between both beams corresponds to $\frac{\pi}{4}$ as it is illustrated in Fig. 4.2

4.2 Stability and temporal drifts

Measurements, which are based on a quadrature signal, require that the overall phase $\Phi(t)$ between both signals is kept constant and the quadrature condition of a phase delay of $\frac{\pi}{2}$ is fulfilled. In order to test the stability of the signal from the setup presented in Fig.4.1 I recorded the temporal evolution of the quadrature signal for a time interval of eight minutes. At the beginning of the measurement I aligned the signals such that they were in quadrature. Thus, if the overall phase is changing, the temporal evolution should be traced along the circumference of a circle (c.f. Fig.2.5). For the following considerations I(t) and Q(t)are expressed in terms of the interference contrast V. This yields,

$$I(t) = I_1 + I_2(1 + V\cos(\Phi(t))) \tag{4.4}$$
$$Q(t) = I'_1 + I'_2(1 + V'\sin(\Phi(t) + z(t))),$$

where the prime indicates that the interference constrast and the intensities of each interferometer arm with intensity I_1 and I_2) can differ between both quadrature components. The
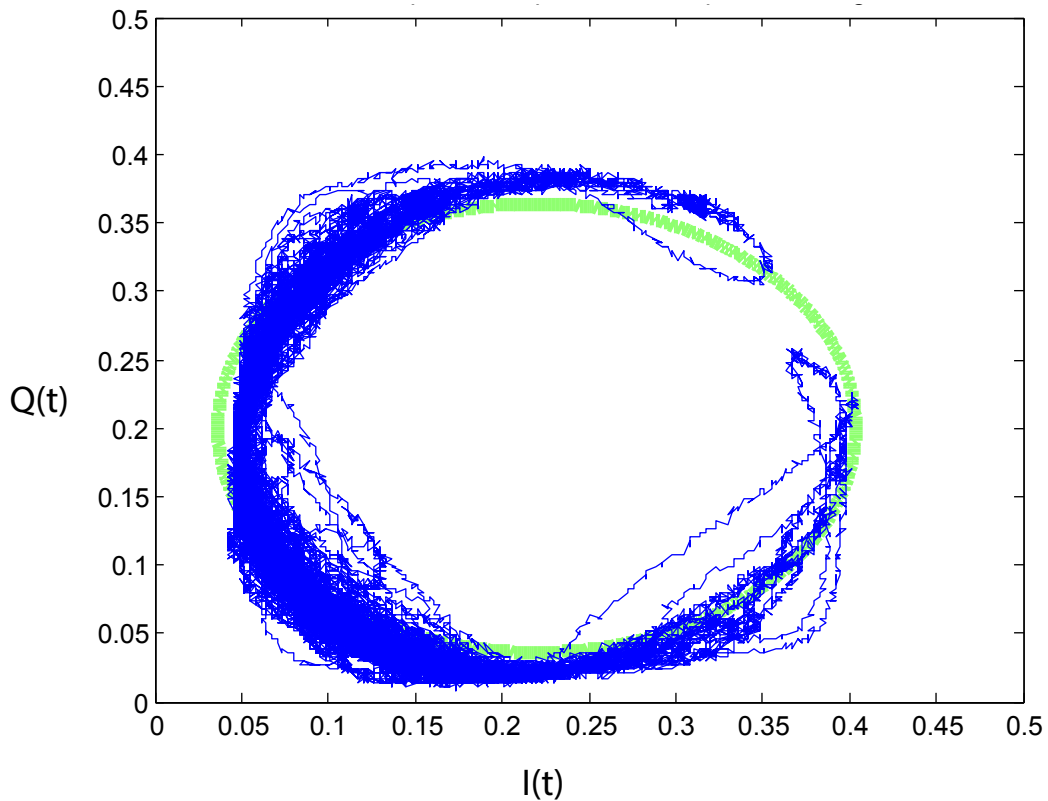
Fig. 4.3: Measurement of the temporal drifts of the quadrature signal. The signal is drifting along an elliptical trajectory. Fluctuations in the amplitude of I(t) (Q(t)) lead to the broadening of the line in both directions. The signals are not in quadrature which leads to the elliptcal shape and the offset from the zero line.

sum of the intensities determines an total offset for the center position of the circle (ellipse) as one can see in Fig.4.3. Therefore, the center position is shifted. Two kinds of fluctuations which can be also seen in Fig. 4.3 contribute. They lead to a deviation from the ideal circular shape and to drifts of the quadrature signal along the circular (elliptical) trajectory. First, the path length difference $\Delta s = s_2 - s_1$ (Fig.2.14) can change by mechanical vibrations of the optical mounts or table for instance. This affects both components equally and leads to a drift along the trajectory. It is denoted by $\Phi(t)$ in Eq.4.4 In addition the relative phase delay between both quadrature components could be modulated by modulations of the tilts of the glas plate. This is denoted by $z(t)$ and leads to an elliptical shape since it adds an additional phase delay. In Fig.4.3 the corresponding measurement of temporal drifts is shown. The piezo mirror was fixed at one position. In this time interval the total phase of the quadrature components, as it is denoted by $\Phi(t)$ in Eq.4.4, was drifting almost by a whole period . The offset for Q and I differs because the intensities of Q(t) are lower due to additional transmission losses in the glass plate (c.f Fig.2.14.). This is underlined by fitting an ellipse

to the measured data. The fitted values yielded:

Center values

$I_0 = (0.23 \pm 0.01)$

$Q_0 = (0.20 \pm 0.01)$

$I_{\text{max}} = (0.19 \pm 0.01)$

$I_{\text{max}} = (0.16 \pm 0.01)$

This measurement shows that the quadrature signal is sensible to fluctuations such as mechanical vibrations. Thus, the phase of each quadrature component should be stabilized further. The stability of the relative phase delay could be increased by replacing more mounts of the involved optics to high stability mounts and using a monolithic cube for the interferometer(c.f Sec.3.3). The temperature dependence of the phase delay by thermally induced changes of the path length difference Δl should be examined as well in the future.

4.3 Considerations for experimental realization in SDT

Referring to the experimental apparatus in Fig. 4.1. one has to consider several aspects:

- Both the σ^+ and a σ^- polarized components of the state dependent optical lattice have to be controlled individually. This means that the circular polarization components of DT1 (DT1R and DT1L, [50]) have to be adjusted by a waveplate such that they can be overlapped with the linear polarized arm of DT2.

- Distortions of the polarization purity by transmission and reflection at the glass plate have to be compensated by an additional correction waveplate

- The quadrature signals from the σ^+ and the σ^- polarized optical lattice should be independent from each other.

- The space is limited. Hence the setup should be designed as compact as possible.

4.4 Outlook

As shown in Fig.4.3 a quadrature signal, where the components I(t) and Q(t) represent an interference signal, is rather sensitive to fluctuations. Therefore first the stability of the quadrature signal has to be increased. Then, referring to the conditions listed above, the presented setup(Fig.4.1) can be extended in order to test the creation of a quadrature signal for different circular polarizations. Accordingly the laser beam from the Littrow laser should be divided by a beam splitter to realize two counterpropagating arms which are superimposed at both sides of the glass plate (c.f. Fig.4.2). Adjusting the polarisations and inserting the waveplate as suggested the realization of a quadrature interferometer in our experiment can be tested.

5

Conclusion and Outlook

The preparation of atoms in the three dimensional motional ground state is a prerequisite for the realization of a controlled interaction between two massive, bososnic particles. The interaction phase the atoms accumulate is well defined and reproducible in this case. Microwave sideband cooling is not possible in the radial plane of the optical trapping potential since it requires a relative spatial displacement between the state dependent potentials. [25, 23] Therefore a setup for cooling into the radial plane using Raman transitions on the first blue sideband has been assembled which I presented in chapter 2. I contributed by characterizing the phase noise from the optical phase lock loop (OPLL) of the Raman setup. Raman sidebands transitions between two hyperfine ground states require a stable phase relation between the two driving lasers. Therefore the OPLL was used to stabilize the phase between the Raman lasers. For the characterization the intensity spectrum of the OPLL was measured. An integration yielded that $(99.91 \pm 0.01)\%$ of the total power are stored below the carrier. The signal-to-noise amplitude is 90 dB (c.f Sec.2.4.4). In addition, the phase noise was directly measured in a quadrature measurement. I obtained a value of $\phi_{RMS} = (0.033 \pm 0.001)$ rad. A calculation of the portion of the total power below the carrier from that value(Eq.2.47) showed a good accordance to the value calculated from integration. It is $P_{\text{Quadr.}} = (99.89 \pm 0.01)\%$. By means of this Raman setup it is possible to cool the atoms into the motional ground state with a probability of $P_0 = (50 \pm 6)\%$, now.

In order to gain more knowledge about the 'errorbudget', which means limiting factors such as differnt sources of noise ([29, 28]) of our experimental apparatus I focused on the characterization of the common mode optical phase noise from the optical lattice in the second part. However, next to the realization of the three dimensional ground state, that is to reduce heating from noise as well, a high accuracy in the reconstruction of the positions from the fluorescence images is necessary. The planned controlled interaction has to take place in the same lattice site. For the fast fluctuations we supressed the slow drifts by a feedback loop and took a power spectral density spectrum. From that spectrum the RMS phase noise of the fast fluctuating component could be determined. It is (44 ± 5) pm and thus four orders of magnitude smaller than one lattice site of $d = 433$ nm. However, considering displacements for times of 4s and 36s respectively showed that without the feedback loop the slow drifts influence the position reconstruction for the longer time interval. Accordingly the feedback loop stabilized the optical lattice for this drift. The distribution of the displacements is then comparable to the case of 4s(c.f Fig.3.15). An extension of the phase noise interferometer to a quadrature interferometer could allow to monitor directly the temporal evolution of the phase noise of both lattice potentials independently and in a long term goal used for a stabilization of the fast fluctuating component. Therefore in Ch.4 a first test was shown. It revealed that a measurement of two interference signals in quadrature configuration is rather sensitive to mechanical fluctuations for example.

The characterization of two different kinds of phase noise for the preparation of atoms in the motional ground state shows that it is of importance to consider all aspects of an experiment. That is assembling the general experimental apparatus for the realization of physical processes such as a phase lock loop to sucessfully drive Raman sideband transitions and to gain knowledge about the limitations of our measurement. Then, the combination of an experimental apparatus with a control over limiting effects such as noise improves the accuracy of a measurement of a physical quantity.

By preparing 56% of the atoms in the ground state an important barrier for the demonstration of the Huong-Ou-Mandel effect with indistinguishable, bosonic atoms, has been broken down. The combination of that with the progress which has been made by other members of our group regarding the transport of two atoms to the same lattice site made conduction of this experiment in principle possible. Further we came closer to the realization of entangled states of neutral atoms via cold collisison as it has been first proposed theoretically in 1999 [20]. Entangled states are essential on the route of simulating physics with quantum computers as it has been proposed by Richard Feynman in 1982 [17].

According to the huge progress since 1982 further progress may be made in the following years. Hopefully, it will give us a deeper insight into the very nature of quantum mechanics and the ability to use the control in the microscopic regime for the macroscopic world.

6

Appendix

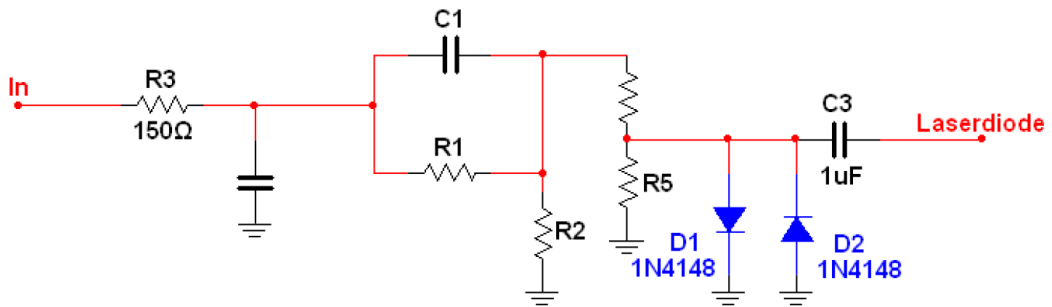## 6.1   Schematic of Lead-Lag Filter in OPLL

Fig. 6.1: Schematics of the Lead Lag Filter which increases the bandwidth of the OPLL, i.e
compensates signals which are up to $1.5\,\mathrm{MHz}$ away. This is indicated by the
servobumps at this freqency(c.f Fig.**??**. Schematics are after [47, 48]

The optimal values have been found by my collegue Ricardo Gomez and are the following.

C_1	$22\,\mathrm{pF}$
C_2	$22\,\mathrm{pF}$
C_3	$1\,\mu\mathrm{F}$
R_1 (P)	$\approx 10\,\mathrm{k}\Omega$
R_2(P)	$334\,\Omega$
R_3	$150\,\Omega$
R_4-R_5 (P)	$(354\,\Omega,68\,\Omega)$
Potentiometer$\equiv$ P	

Tab. 6.1: Values of the Lead Lag Filter, which has been used in the OPLL in Ch.2, Sec.2.4.2
By means of this the bandwidth of the OPLL is increased, such that the servo bumps occur
at a frequency of $1.5\,\mathrm{MHz}$ now.

6.2 Relation between fraction of total power below carrier and RMS phase noise

Here I am following the approach presented from Ref.[49] and references therein. The electric field of a single mode laser in the presence of phase and amplitude noise can be described by:

$$E(t) = \varepsilon(t)e^{-i\omega_0 t - i\phi_N t}, \tag{6.1}$$

where $\varepsilon(t)$ denotes the field amplitude and ϕ_N the (phase) noise. Generally the autocorrelation function is defined as:

$$C_\chi(\tau) = \langle \chi(t)\chi^*(t+\tau)\rangle \tag{6.2}$$

One can express $\varepsilon(t)$ in terms of the noise amplitude $V_N(t)$,

$$\varepsilon(t) = \begin{cases} E_0[1+V_N(t)] & V_N(t) \geq -1 \\ 0 & V_N(t) \leq -1 \end{cases}$$

and use the Wiener-Khintchine theorem which states that the Fouriertransform of the power spectral density, e.g the fraction of total power per frequency interval corresponds to the autocorrelation functin [9]. The assumption that there exist no correlations between the noise due to amplitude and phase fluctuations and $\mathrm{Var}(V_N(t) \ll 1)$ leads to a simplified expression of the autocorrelation function.

$$C_{E(\tau)} = E_0^2 e^{i\omega_0\tau}\{1 + \langle V_N(t)V_N(t+\tau)\rangle\} \cdot \langle e^{i(\phi_N(t+\tau)-\phi_N(t))}\rangle \tag{6.3}$$

The autocorrelation function of the different noise sources is defined as $C_\phi(\tau)$ for the phase and $C_V(\tau)$ for the amplitude noise respectively. According to the Gaussian moment theorem [58] one can write,

$$\langle e^{i(\phi_N(t+\tau)-\phi_N(t))}\rangle = e^{-\Omega_\phi(\tau)}, \tag{6.4}$$

with

$$\Omega_\phi(\tau) = C_\phi(\tau) - C_\phi(0),$$

which yields:

$$C_E(\tau) = E_0^2 e^{i\omega_0\tau} e^{-\Omega_\phi(\tau)}\{1 + C_V\} \tag{6.5}$$

The total power is calculated by integration of the power spectral density over the whole spectrum and exploiting the linearity of the Fourier transform yields:

$$P = \int_{-\infty}^{\infty} S_E(\omega)d\omega = C_E(0) = E_0^2\{1 + C_V\} \tag{6.6}$$

In the limit of $\tau \to \infty$ the power which remains in a certain frequency interval corresponds to the fraction of total power and assuming the amplitude fluctuations vanishes as well the phase noise, attributed by $\Omega_\phi(\tau)$, is the dominating contribution.

In this limit the autocorrelation function of the phase corresponds to the one of the noise and one obtains:

$$\lim_{\tau\to\infty} C_E(\tau) = E_0^2 e^{-C_\phi(0)} e^{i\omega_0\tau} \tag{6.7}$$

$$= E_0^2 e^{-\langle\phi_{RMS}^2\rangle} e^{i\omega_0\tau}$$

Thus the fractional power in a certain frequency interval,e.g below the carrier, can be obtained from:

$$\frac{P}{P_{total}} = S_E(\omega) = e^{-\langle\phi_{RMS}^2\rangle} \tag{6.8}$$

6.3 Required sensitivity for quadrature interferometer
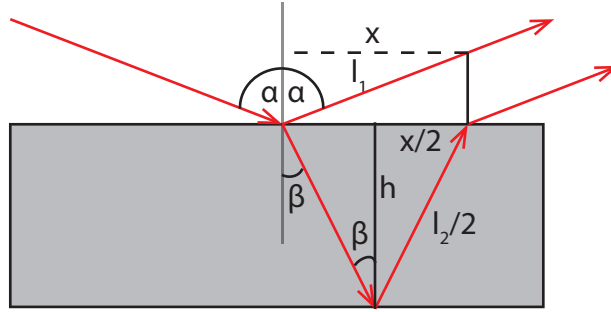

Fig. 6.2: Illustration for the relations used below. There α denotes the incidence angle, h the thickness of the glassplate, β the angle in the glassplate, l_1 and l_2 the different path lengths.

In order to calculate the sensitivity, we will derive an expression for the relative change in $\Delta l = l_2 - l_1$ with respect to the incidence angle. That is $\frac{\partial \Delta l}{\partial \alpha}$. Therefore taking small tilts into accound the incidence angle is

$$\gamma = \frac{\pi}{4} + \delta\alpha \tag{6.9}$$

Using Snell's law [53] the path lengths and thus Δl be expressed as:

$$l_1 = 2h\frac{\tan(\beta)}{\sin(\gamma)} = \frac{2h}{n\cos\beta}$$

$$l_2 = \frac{2hn}{\sin(\gamma)}\tan(\beta)$$

For small fluctuations we can use:

$$\cos(\beta) = \sqrt{1 - \frac{\sin^2(\alpha)}{n^2}} \approx \sqrt{1 - \frac{1}{n^2}(1+2\delta\alpha)}$$

$$\frac{1}{\sqrt{1-x}} \approx 1 + \frac{1}{2}x + \mathcal{O}(x^2)$$

This yields for the path length difference in first order of the small fluctuation:

$$\Delta l = 2h\left(1 - \frac{1}{n}\right)\left(1 + \frac{1}{2n^2}\left(\frac{1}{2}(1+2\delta\alpha)\right)\right)$$

Consequently derivating that expression yields:

$$\frac{\partial \Delta l}{\partial \delta\alpha} = \frac{2h}{n^2}\left(1 - \frac{1}{n}\right) \tag{6.10}$$

Acknowledgments

64

Bibliography

[1] Encyclopaedia Britannica Inc. Encyclopaedia britannica online academic edition0. <http://www.britannica.com/EBchecked/topic/458757/physics>, 2014. Web, September,28, 2014.

[2] W. I. Berveridge. *The Art of Scientific Investigation*. Heinemann, 1950.

[3] International Organization for Standardization (ISO). Guide to the expression of uncertainty in measurement, 1993.

[4] M. Young. *Optics and Lasers*. Springer Verlag, 2000.

[5] M. A. Nielsen and I. L. Chuang. *Quantum Computation and Quantum Information*. Cambridge University Press, 2000.

[6] H. A. Bachor. *A Guide to Experiments in Quantum Optics*. WILEY-VCH, 1998.

[7] E. Rubiola. *Phase Noise and Frequency Stability in Oscillators*. Cambridge University Press, 2008.

[8] R.Paschotta. Noise in laser technology-part 1: -intensity and phase noise. *Optik und Photonik*, 48, 2009.

[9] Amnon Yariv. *Optical Electronics in Modern Comunications*. Oxford University Press, Inc., 1997.

[10] P. D. Drummond and M. Hillery. *The Quantum Theory of Nonlinear Optics*. Cambridge University Press, 2014.

[11] K. Blum. *Density Matrix Theory and Applications*. Springer Verlag, 2012.

[12] R. Blatt and C.F. Roos. Quantum simulation with trapped ions. *Nature Phys.*, **8**:277–284, 2012.

[13] S. Chu et al. Three-dimensional viscous confinement and cooling ofatoms by resonance radiation pressure. *Phys. Rev. Lett.*, **55**, 1:48–51, 1985.

[14] M. Karski et al. Quantum walk in position space with single optically trapped atoms. *Science*, **325**,174, 2009.

[15] M. Greiner et al. Quantum phase transition from a superfluid to a mott insulator in a gas of ultracold atoms. *Nature*, **415**,39-44, 2002.

[16] M. Kasevich and S. Chu. Laser cooling below a photon recoil with three level atoms. *Phys. Rev. Lett*, **69**,12, 1992.

[17] R. Feynman. Simulating physics with computers. *Int. Journ. Theo. Phys.*, **21**, 1982.

[18] A. Alberti. Quantum statistics with exactly two atoms.

[19] C.K. Hong et al. Measurement of subpicosecond time intervals between two photons by interfernce. *Phys. Rev. Lett.*, **59**,18, 1987.

[20] D. Jaksch et al. Entanglement of atoms via cold controlled collisions. *Phys. Rev. Lett.*, **82**,1975-1978, 1999.

[21] D. Schrader et al. Neutral atom quantum register. *Phys. Rev. Lett.*, **93**,15, 2004.

[22] I. Bloch et. al. Quantum simulations with ultracold quantum gases. *Nature Physics*, **8**, 2012.

[23] L. Förster. *Microwave control of atomic motion in a spin dependent optical lattice.* PhD thesis, Rheinische Friedrich - Wilhelms Universität Bonn, 2010.

[24] H.-J. Briegel et al. Quantum computing with neutral atoms. *J.Mod. Opt.*, **47**,213:415–451, 2000.

[25] L.Förster et al. N.Belmechri. Microwave control of atomic motional states in a spin dependent optical lattice. *J. Phys.B: At.Mol.Opt. Phys.*, **46**,104006, 2013.

[26] S. Kuhr. *A controlled quantum system of individual neutral atoms.* PhD thesis, Rheinische Friedrich - Wilhelms Universität Bonn, 2003.

[27] W.Alt et al. Single atoms in a standing-wave dipole trap. *Phys. Rev. A.*, **67**,033403, 2003.

[28] S.Kuhr et al. Coherence properties and quantum state transportation in an optical conveyor belt. *Phys. Rev. Lett.*, **91**, 21, 2003.

[29] W.Alt. *Optical control of single neutral atoms.* PhD thesis, Rheinische Friedrich - Wilhelms Universität Bonn, 2004.

[30] Z. Y. Ou. Quantum theory of fourth-order interference. *Phys. Rev. A.*, **37**, 5, 1987.

[31] J.H. Eberly L.Allen. *Optical Resonance And Two-Level Atoms.* Dover Publications, Inc., New York, 1987.

[32] Y.B.Ovchinnikov R. Grimm, M. Weidemüller. Optical dipole traps for neutral atoms. *arXiv:physics/9902072*, 1999.

[33] D. Steck. *Quantum and Atom Optics.* available online at http://steck.us/teaching, (revision 0.9.13,26 August 2014).

[34] G. Münster. *Quantentheorie.* Walter de Gruyter GmbH and Co. KG,Berlin/New York, 2010.

[35] H.J.Metcalf and P.v.d. Straaten. *Laser Cooling and Trapping.* Springer Verlag New York, 1999.

[36] I.I.Sobelman. *Atomic Spectra and Radiative Transitions.* Springer, New York, 1979.

[37] Daniel. A. Steck. **Cesium D Line Data**. *available online at http://steck.us/alkalidata*, revision 2.1.4, Dec. 2010.

[38] M. Karski. *State-selective transport of single neutral atoms.* PhD thesis, Rheinische Friedrich - Wilhelms Universität Bonn, 2010.

[39] I. Dotsenko. Raman spectroscopy of single atoms. Master's thesis, Rheinische Friedrich - Wilhelms Universität Bonn, 2002.

[40] Leibfried et al. Quantum dynamics of single trapped atoms. *Reviews of modern physics*, 75, 2003.

[41] D.J Wineland and W.M. Itano. Laser cooling of atoms. *Phys. Rev. A*, 20, 1979.

[42] D.Kielpinski et al. Q.A. Turchette. Heating of trapped ions from the quantum ground state. *Phys. Rev. A*, **61**,063418, 2000.

[43] L. H. Pedersen E. Brion and K. Mølmer. Adiabatic elimination in a lambda-system. *J. Phys. A: Math. Theor.*, **40**,1033, 2007.

[44] S.Hild. Resolved raman sideband cooling in a doughnut-shaped optical trap. Master's thesis, Rheinische Friedrich - Wilhelms Universität Bonn, 2011.

[45] A. Mawardi. Generation of a donut beam for a tight radial confinement of atoms in a one-dimensional optical lattice. Master's thesis, Rheinische Friedrich - Wilhelms Universität Bonn, 2010.

[46] E. Hecht. *Optik*. Oldenbourg Verlag München Wien, 2005.

[47] K.Schorner. Ein phasenstabilisiertes lasersystem fÃ$\frac{1}{4}$r resonatorinduzierte raman-prozesse. Master's thesis, Rheinische Friedrich - Wilhelms Universität Bonn, 2008.

[48] M.Prevedelli et al. Phase locking of grating tuned diode lasers. *Appl. Phys. B*, **60**,241, 1995.

[49] M.Zhu and J.L.Hall. Stabilization of optical phase/freqeuncy of a laser system: application to a commercial dye laser with an external stabilizer. *J. Opt. Soc. Am. B*, **10**,802, 1998.

[50] A.Hambitzer. Direct synthesis of light polarization for state-dependent transport. Master's thesis, Rheinische Friedrich - Wilhelms Universität Bonn, 2012.

[51] Thomas C. OHaver. peakfit.m. http://www.mathworks.com/matlabcentral/fileexchange/23611-peak-fitter, 2013. Last accessed September,28, 2014.

[52] M.Michelson and E.A.Morley. On the relative motion of the earth and the luminiferous ether. *American Journal of Science*, 34(203):333–345, 1887.

[53] W.Demtröder. *Experimentalphysik 2: Elektrizität und Optik*, volume 6. Springer Verlag, 2013.

[54] D.Meschede. *Optik, Licht und Laser*, volume 1. B.G.Teubner Stuttgart, 1999.

[55] S. Aris. *Probability Theory and Statistical Inference*. New York Cambridge University Press, 1999.

[56] K.F.Riley. *Mathematical methods for the Physical Sciences*, volume 1. Cambridge University Press, 1974.

[57] M. J. Nasse and J.C. Woehl. Realistic modeling of the illumination point spread function in confocal scanning optical microscopy. *J. Opt. Soc. A.*, **27**, 2, 2010.

[58] I. Reed. On a moment theorem for complex gaussian processes. *IRE Trans.*, **8**,3, 1962.

Erklärung der Selbstständigkeit

I hereby certify that the work presented here was accomplished by myself and without the use of illegitimate means or support, and that no sources and tools were used other than those cited.

Bonn, September 29th, 2014